Catal Surv Asia (2012) 16:210–230
DOI 10.1007/s10563-012-9145-0

Morphology-Controlled Synthesis and Applications of Silver Halide Photocatalytic Materials

Baozhu Tian · Jinlong Zhang

Abstract Semiconductor photocatalysis is considered to be one of the most promising technologies to solve the worldwide environmental and energy issues. In recent years, silver halide (AgX)-based photocatalytic materials have received increasing research attention owing to its excellent visible light-driven photocatalytic performances in the applications of organic pollutant degradation, H_2/O_2 generation, and disinfection. AgX-based materials used in photocatalytic fields can be classified into three categories: AgX (Ag/AgX), AgX composites, and supported AgX materials. For the AgX (Ag/AgX) photocatalysts, it has been widely accepted that the final photocatalytic performances of photocatalysts are severely dependent on their morphological structures as well as exposed crystal facets. As a result, considerable efforts have been devoted to fabricating different morphological AgX photocatalysts as well as exploring the relationship between the morphological structures and photocatalytic performances. In this review, we mainly introduce the recent developments made in fabricating morphology and facet-controllable AgX (Ag/AgX) photocatalytic materials. Moreover, this review also deals with the photocatalytic mechanism and applications of AgX (Ag/AgX) and supported AgX materials.

Keywords Silver halide · Photocatalytic materials · Morphological structures · Surface plasmon resonance · Photocatalytic performance

1 Introduction

Since the discovery of photoelectrochemical splitting of water on n-TiO_2 electrodes [1], semiconductor photocatalysis has received increasing attention as a promising technologies to solve the worldwide energy crisis, environmental pollution, and global warming via hydrogen generation by water splitting [2–4], degradation of environmental pollutants [5–7], and conversion of carbon dioxide into gaseous hydrocarbons [8, 9]. Amongst various semiconductor materials, TiO_2 has been widely studied due to its excellent optical and electronic properties, low cost, chemical stability and nontoxicity [10, 11]. However, there are two issues for its practical applications, one of which is to improve the low photo-quantum efficiency of TiO_2 that arises from the fast recombination of photoinduced electrons and holes; the other is to further extend its photoresponse in visible light regions. To meet the requirements of future environmental and energy technologies driven by solar energy, the exploitation of more efficient sunlight active photocatalysts has become the most important subject of photocatalysis research.

Silver halides (AgX) are well-known as photosensitive materials and widely used in various photographic films. The photographic process in AgX is as follows: After absorbing a photon, silver halide can produce an electron and a hole, and subsequently the electron combines with an interstitial silver ion to form an Ag^0 atom. Upon repeated absorption of photons, a cluster of silver atoms will be formed ultimately [10, 11]. Generally, the critical size of silver clusters for forming latent image is considered to be

B. Tian · J. Zhang (✉)
Key Laboratory for Advanced Materials and Institute of Fine Chemicals, East China University of Science and Technology, 130 Meilong Road, Shanghai 200237, People's Republic of China
e-mail: jlzhang@ecust.edu.cn

B. Tian
e-mail: baozhutian@ecust.edu.cn

four silver atoms [11]. Due to the instability under light, silver halides are seldom used as photocatalysts previously.

In 1996, Calzaferri et al. [12] reported that thin silver chloride layers on SnO_2-coated glass plates evolved O_2 in the presence of small excess Ag^+ ions, which opened the door of researching the photocatalytic performance of AgX materials. In 1999, Kakuta et al. [10] found that AgBr dispersed on SiO_2 support can continuously produce H_2 for 200 h without composition destruction. Subsequently, supported and composite AgX photocatalysts such as $AgCl/Al_2O_3$ [13], $Ag/AgCl/TiO_2$ [14], $AgBr/TiO_2$ [15], AgBr/Al-MCM-41 [16], and AgI/TiO_2 [17] have been successfully used in pollutant degradation, NO_x conversion, and sterilization [13–17]. It was widely accepted that the metallic Ag formed on the surface of AgX can separate electron–hole pairs by forming Schottky barrier, which not only enhancing photocatalytic activity but also improves the stability of AgX [15]. In addition, both of composites and supported structures are also beneficial to the improvement of photocatalytic activity and stability [10, 15, 18–20].

Noble metal nanoparticles, such as Au, Ag, Pt, and Cu, exhibit strong UV–Vis absorption due to their surface plasmon resonance (SPR) [21]. As a result, plasmonic NPs can serve as an alternative type of sensitizers to enhance the visible light absorption of photocatalysts without the trouble of degradation like organic sensitizers [22, 23]. In 2008, Huang et al. [24] fabricated Ag/AgCl plasmonic photocatalyst by an ion-exchange method, which triggered an upsurge of researching Ag/AgX plasmonic photocatalsts.

At present, AgX-based materials used in photocatalytic fields can be classified into three categories: AgX (Ag/AgX), AgX composites, and supported AgX materials. For the AgX (Ag/AgX) photocatalytic materials, it has been confirmed that the final photocatalytic performances of AgX are severely dependent on their morphological structures as well as exposed crystal facets. Many methods such as ion exchange reaction [24, 25], Ag-engaged galvanic replacement [26, 27], electrospinning [28], double-jet precipitation [29], microemulsions [30, 31] have been employed to fabricate AgX materials. Until now, AgX photocatalysts with various morphologies such as nanowires [26, 27], nano- or microcubes [21, 31], micospheres [32], and porous structures [33] have been successfully fabricated. In addition, AgX nano- or microcrystals with exposed highly reactive facets also have been synthesized by employing suitable capping agent and controlling the release rate of Ag^+ or X^- ions [34, 35]. In this review, we mainly introduce the recent advances made in fabricating morphology and facet-controllable AgX (Ag/AgX) photocatalytic materials. Moreover, this review also deals with the photocatalytic mechanism and applications of AgX (Ag/AgX) and supported AgX materials.

2 Morphology and Facet-Controlled Synthesis of AgX (Ag/AgX) Photocatalytic Materials

2.1 Ag/AgX Nanowires

1D semiconductor nanostructures such as rods, wires, and tubes, have attracted extensive attention owing to their unique electronic and optoelectronic properties, as well as potential applications in fabricating nanoscale devices [36–39]. As photocatalytic materials, 1D semiconductor nanostructures often show higher photocatalytic performance compared with nanoparticles because their higher surface-to-volume ratio would guarantee a high density of active sites available for surface reactions as well as a high interface charge carrier transfer rate [40, 41]. Normally, the solution-phase routes for fabricating 1D semiconductor nanostructures can be classified into two categories [36]: (1) the routes involving solid templates or substrates, such as the chemical transformation of 1D sacrificial templates and the oriented growth of 1D nanostructures on solid substrates [42, 43]; (2) the routes based on controlled precipitation from homogeneous solutions, such as hydrothermal/solvothermal [44, 45] and solution-liquid–solid process [46]. To date, various photocatalytic materials with 1-D structures such as TiO_2 [41, 47], ZnO [48, 49], CuO [50], CeO_2 [51], Ta_2O_5 [52], CdS [53], Bi_2S_3 [54], Sb_2S_3 [55], ZnSe [56], and $BiVO_4$ [57] have been successfully synthesized.

Ag-engaged galvanic replacement has been proved to be a versatile chemical transformation method for fabricating hollow metal nanostructures such as Pt, Au, and Pd [58–61]. Recently, this technique has been successfully employed to construct AgCl and AgBr nanowires [26, 27, 62–64]. The standard redox potential of Ag^+/Ag couples is 0.80 V (vs. standard hydrogen electrode, SHE), while that of Fe^{3+}/Fe^{2+} is 0.771 V [26]. Normally, metallic Ag cannot be oxidized to Ag^+ ions by Fe^{3+} ions. However, in the presence of X^- ions, the redox potential of Ag species is reduced from 0.80 V for Ag^+/Ag (vs. SHE) to lower value for AgX/Ag due to the very low solubility product constants of silver halide (AgX) (at 25 °C, $k_{sp,AgCl} = 1.8 \times 10^{-10}$, $k_{sp,AgBr} = 5.0 \times 10^{-13}$, and $k_{sp,AgI} = 8.0 \times 10^{-17}$). For instance, the redox potentials for AgCl/Ag and AgBr/Ag are 0.223 V and 0.007 V (vs. SHE), respectively [28, 62, 63]. By contrast, the redox potential of Fe^{3+}/Fe^{2+} keeps constant at 0.771 V (vs. SHE) regardless of the concentration of X^- ions. The difference of the redox potentials between AgX/Ag and Fe^{3+}/Fe^{2+} couples provides the driving force for the replace reaction, in which X^- ions not only serves as a halide source for the growth of AgX nanocrystals but also as an activation agent to initiate the replacement reaction (Eq. 1).

$$Ag + FeX_3 \rightarrow AgX \downarrow + FeX_2 \quad (1)$$

Ag nanowires are usually employed as template for the synthesis of Ag/AgX nanowires or core–shell nanowires [26, 27, 63, 64]. For instance, Ye et al. [26] synthesized Ag/AgCl core–shell nanowires via the replacement reaction between Ag nanowires and $FeCl_3$ solution (Fig. 1). Polyvinyl pyrrolidone (PVP) was found to play a vital role in determining the morphological structures of the AgCl shells. In the presence of PVP, uniform and smooth Ag/AgCl core–shell nanowires can be formed were produced, while the products were transformed into irregular rod-like structures with rough nanoshells in the absence of PVP. The photocatalytic degradation of methyl orange (MO) dye indicated that Ag/AgCl core–shell nanowires with 8:92 ratio (Ag:AgCl) exhibit the highest activity than other core–shell and pure AgCl nanostructures (almost MO was 100 % degraded after visible light irradiation for 8 min).

The thickness of AgCl shells can be adjusted by changing the molar ratio of $FeCl_3$ to Ag. Li et al. [63] found Ag nanowires can be transformed into AgCl nanowires completely when the molar ratio of Fe:Ag was increased to 6:5. By reducing $NaAuCl_4$ with Fe^{2+} ions generated in the formation of AgCl nanowires, Sun et al. [62] prepapred Au nanoparticle-decorated AgCl nanowires, which exhibited highly photocatalytic activity for the degradation of MB under visible light irradiation. Analogously, Ag/AgBr core–shell nanowires can be obtained by using $FeBr_3$ instead of $FeCl_3$ [64].

Ag foils also can be used as Ag source to synthesize Ag/AgX (X = Cl, Br) nanowires. By galvanic replacement method, Ye et al. [27] successfully synthesized high aspect ratio AgBr nanowires with lengths of several tens micrometers and diameters of ~70 nm on the surface of Ag foils. In this system, PVP molecules were selectively adsorbed onto the certain crystal facets of AgBr nanocrystals, which may change their growth rates and induce the oriented attachment of the AgBr nanocrystals into 1D nanowires on Ag substrates. The growth process of AgBr nanowires on Ag substrates is illustrated in Scheme 1. Firstly, uniform AgBr nanocrystals with octahedron-like tructures were formed on the surfaces of Ag foils. Subsequently, AgBr nanocrystals attached to each other and self-assembled into tower-like nanostructure arrays. Finally, AgBr nanostructure arrays grew into AgBr nanowires. Photocatalytic degradation of MO indicated that AgBr nanowires exhibited higher photocatalytic activity than AgCl nanowires and AgBr nanoparticles.

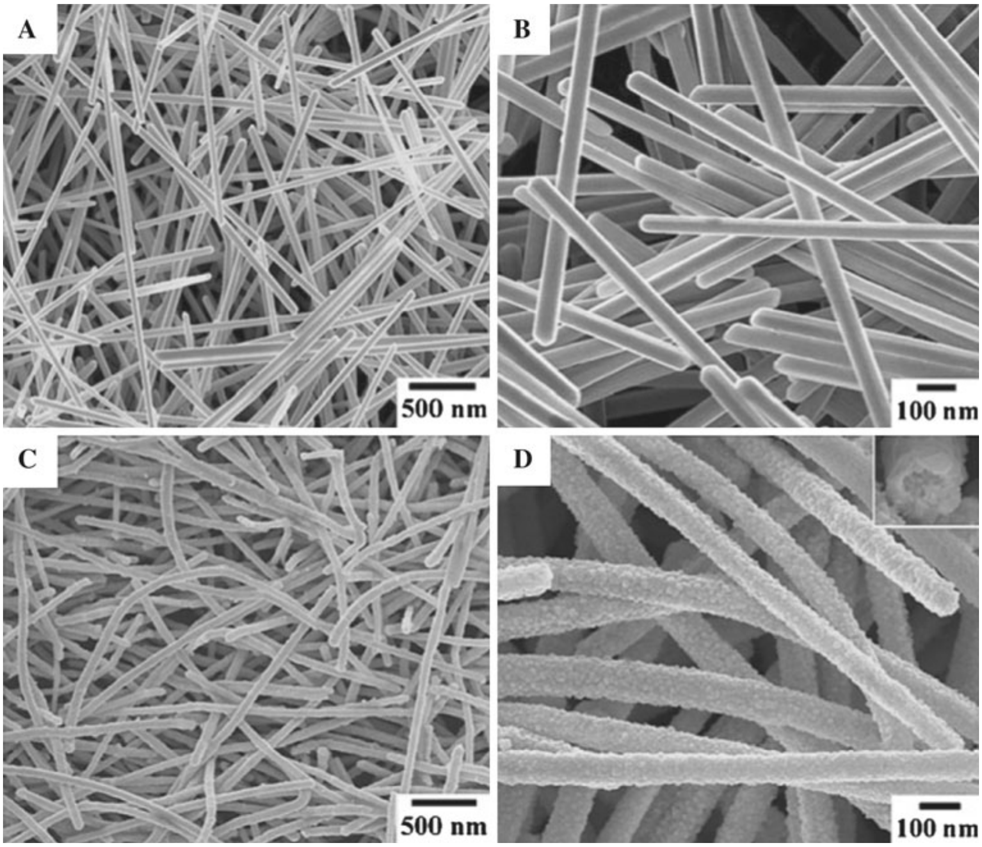

Fig. 1 SEM images of Ag nanowires (**a**, **b**) and Ag/AgCl core–shell nanowires (**c**, **d**) [26]

Scheme 1 Schematic illustration of the heteroepitaxial growth process of AgBr nanowires on Ag substrates [27]

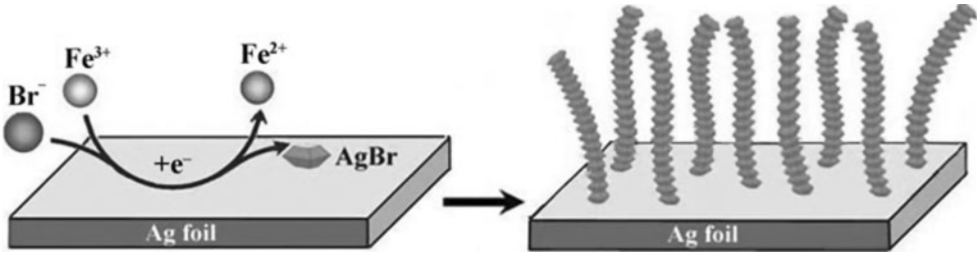

2.2 Cubic/Semi-Cubic Ag/AgX

Semiconductor photocatalysts with cubic shape have various merits such as higher specific surface area, more active sites, and active facets, compared with their spherical counterparts with a similar size [30, 65, 66], all of which are favorable to the enhancement of photocatalytic activity. Recently, Ag/AgCl plasmonic photocatalyst with cubic morphology has attracted much research interest [30, 31, 67, 68]. Normally, it is hard to well control the morphology of Ag/AgCl due to the high reaction rate between Ag^+ ions and Cl^- ions [31]. Fortunately, cubic Ag/AgCl grains can be successfully constructed by employing polymeric additives such as polyvinylpyrrolidone (PVP) as morphology-directing agents [30, 31, 67, 68]. To date, several synthetic methods such as microemulsion [30], hydrothermal/solvothermal [67], sonochemical irradiation [31], and laser ablation [69] have been explored to synthesize cubic Ag/AgCl photocatalyst.

Using PVP as morphology-directing agent, Sun et al. [67] successfully synthesized cube-like Ag/AgCl nanoparticles by a precipitation reaction between Ag^+ and Cl^- ions, followed by hydrothermal treatment in ethylene glycol solution. The obtained cube-like Ag/AgCl plasmonic photocatalyst exhibited high photocatalytic activity and high stability for the decomposition of methylene blue dye under sunlight irradiation. The growth process of AgCl nanocrystals can be divided into three stages [68]: Firstly, Ag^+ ions and PVP molecules can form Ag^+–PVP monomers via electrostatic attraction, and a fraction of Ag^+–PVP monomers nucleate into AgCl nuclei by adding Cl^- ions. Subsequently, AgCl nuclei grow quickly into nanoparticles by consuming the Ag^+ and Cl^- monomers. Finally, the small nanoparticles grow into uniform, larger nanocubes through an Oswald ripening process at the expense of the smaller particles. As mentioned above, high reaction rate between Ag^+ ions and X^- ions is unfavourable for controlling the morphology of AgCl nanocrystals. Using methylene dichloride as chlorine source instead of inorganic chloride source, Dong et al. [68] prepared cube-like Ag/AgCl via a hydrothermal method. In the hydrothermal process, the slow release of Cl^- ions is favourable to the formation of cubic Ag/AgCl morphology.

Cho et al. [31] explored a one-step sonochemical route for synthesizing cube-shaped Ag/AgCl photocatalysts in a PVP–ethylene glycol solution, in which no external heat treatment or reducing agent was employed (Fig. 2). Under ultrasonic irradiation, ethylene glycol can be oxidized into glycolaldehyde which is responsible for reducing Ag^+ into Ag^0. The size of the Ag/AgCl can be tuned by adjusting the concentrations of Ag^+ or PVP, i. e., the size of the Ag/AgCl decreases with the increase of either Ag^+ or PVP concentration. The obtained Ag/AgCl plasmonic photocatalysts show enhanced photocatalytic activity for the degradation of methyl orange (MO), rhodamine B (RhB), and methylene blue (MB) under visible light irradiation.

Microemulsion-based synthesis is a versatile technique to synthesize a variety of nanomaterials, in which the manipulation of various components involved in the formation of a microemulsion enables one to adjust the size and shape of nanomaterials [70]. This technique has also been employed to synthesize morphology and size-controllable Ag/AgCl plasmonic photocatalysts. For instance, An et al. [21] prepared uniform Ag/AgCl nanocubes with an average edge length of 85 nm by a facile reverse micelle method, followed by $NaBH_4$ reduction (Fig. 3). The obtained Ag/AgCl nano-sized photocatalyst exhibits high activity and durability towards degradation of MO. Chen et al. [31] prepared Ag/AgCl plasmonic photocatalysts in an oil-in-water system and investigated the influence of cetyltrimethyl-ammonium concentration in chloroform on the morphology of Ag/AgCl nanopartiles. When concentrated and diluted cetyltrimethyl-ammonium chloride chloroform solutions are employed, sphere-like and cube-like Ag/AgCl nanospecies could be manufactured, respectively. The formation mechanism of Ag/AgCl nanospecies is illustrated in Scheme 2 [31]. When cetyltrimethyl-ammonium chloride chloroform solution is added into $AgNO_3$ aqueous solution, the chloroform phase is dispersed in the water phase, forming a microemulsion system. Nanostructured AgCl comes into being when Ag^+ and Cl^- meet together, wherein the formed AgCl could be partially converted into Ag/AgCl in situ by ambient light. The photocatalytic degradation of MO dye under visible light irradiation indicated that cube-like nanoparticles display much higher photocatalytic activity than the corresponding sphere-like nanoparticles.

2.3 AgX Crystals with Exposed Highly Active Facets

The photocatalytic performance of a photocatalyst is closely related to its exposed crystal facets [71]. Both of theoretical and experimental studies revealed that the facet with a high percentage of under-coordinated atoms possesses higher surface energy and reactivity than that with a low percentage of under-coordinated atoms [71–75]. Unfortunately, the crystal-growing process is apt to diminish the active facets as a result of reducing total surface energy, resulting in low reactive facet percentage in nano- or microcrystals [71, 76]. The terminated facets of nano- or microcrystals can be tailored by two routes, i.e., bottom-up and top-down synthetic methods. For the bottom-up route, the ultimate shape and exposed facets of nano- or microcrystals are usually controlled by adjusting the solvents or additives in solution. The solvent effect on the facets is realized by changing the interactions along different orientations of crystal, while additive effect is to change the relative stability of facets in terms of surface energy. In the case of top-down route, the crystals with designed exposed facets can be obtained by beforehand protecting some surfaces using selective capping agent and subsequently etching other surfaces using etching agent molecules or ions [71].

Since the first successful preparation of anatase TiO_2 single-crystals with 47 % {001} facets by Yang et al. [77] the synthesis of anatase TiO_2 with dominant {001} active facets has become a new research hotspot [78–81]. Recently, relative studies about the synthesis, properties, and applications of {001} facet dominant TiO_2 have been systematically reviewed by two papers [71, 82]. Except for

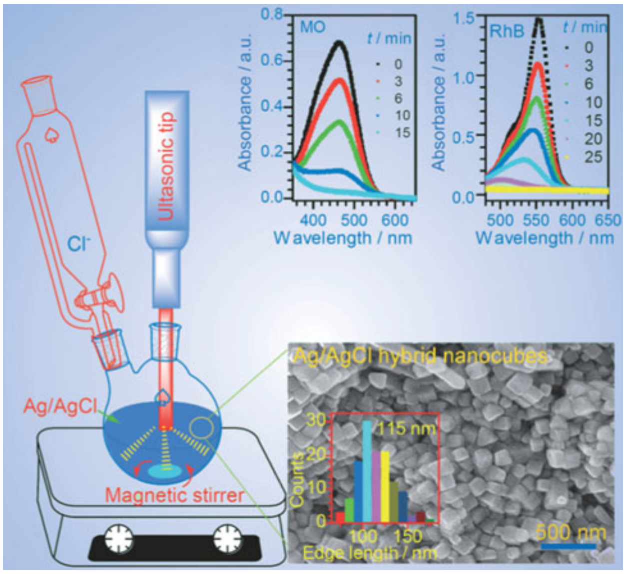

Fig. 2 Schematic diagram of reaction equipment, SEM image of AgCl cubes, and absorbance change of organic dyes as a function of degradation time [31]

Fig. 3 SEM images of the as-synthesized samples and their corresponding size distribution diagrams: **a**, **b** AgCl nanoparticles; **c**, **d** Ag/AgCl hybrid nanoparticles [21]

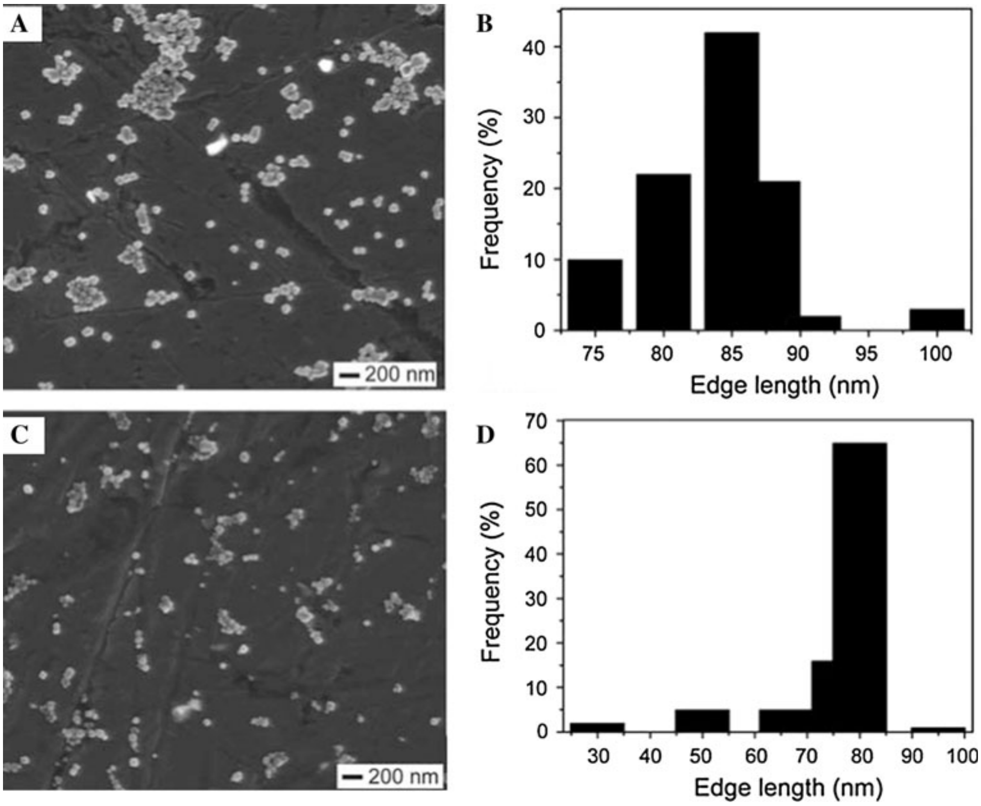

Scheme 2 Possible explanation of the one-pot controllable synthesis of Ag/AgCl-based nanospheres and quasi-nanocubes via an oil-in-water medium [31]

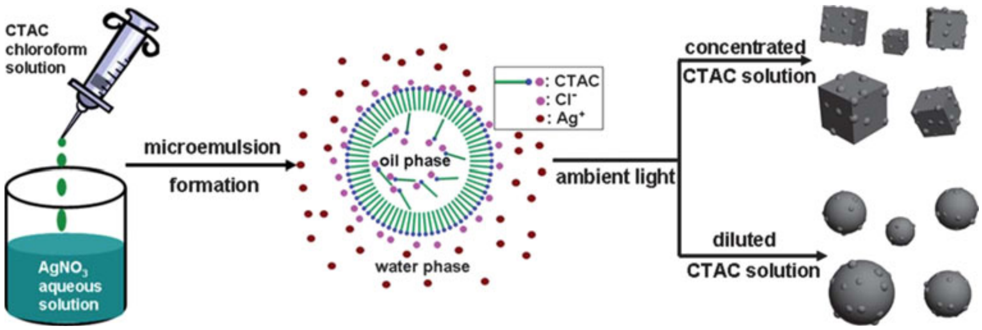

TiO$_2$, other highly active facet dominant photocatalysts such as ZnO [83, 84], Cu$_2$O [85, 86], WO$_3$ [87], and Ag$_3$PO$_4$ [88] also have been fabricated. For instance, ZnO nanodisks with a large percentage of polar (0001) facets and ZnO nanowires with dominant {1010} facets can be readily prepared by simply tuning the synthetic parameters [83]. Ye et al. [88] developed a facile and general route for fabricatiing single-crystalline Ag$_3$PO$_4$ rhombic dodecahedrons with only {110} facets exposed and cubes bounded entirely by {100} facets. It was found that rhombic dodecahedrons exhibit much higher activity than cubes for the degradation of organic contaminants [88].

Recently, the effect of different facets on the photocatalytic performances of AgX photocatalysts has attracted the researchers' attention. The surface energies of AgBr {100} and {110} facets was estimated using Density Functional Theory, to be 0.495 and 0.561 J m^{-2}, respectivey [89]. For AgBr (111) surface, there are two possible structures which would entirely consist of a full layer of either Ag$^+$ or Br$^-$ ions. The total energy calculation indicated that the surface entirely constituted by Ag atoms exhibits the highest stability, implying that the {111} facets are most possibly enclosed by Ag atoms. The surface energy of AgBr {111} facets enclosed by Ag atoms is 1.253 J m^{-2}, which is much higher than that of AgBr {100} and {110} facets, implying that {111} facets are probably more active than {100} and {110} facets in catalytic reactions [89].

The bottom-up synthetic method is usually employed to fabricate highly active facet exposed AgBr crystals. For instance, Li et al. [34, 89] synthesized AgBr tetrakaihecahedrons and nanoplates with exposed {111} facets by a facile precipitation reaction, using PVP as a capping agent. With the increase of PVP dosage, the shape of AgBr evolves gradually from irregular microspheres to tetrakaidecahedrons, mixture of tetrakaidecahedrons and nanoplates, and final regular nanoplates, as shown in Fig. 4. As a non-ionic surfactant, PVP has an easily polarized functional group '–C=O' in its repeated unit, in which 'O', with a negative charge, prefers to interact with positively charged 'Ag' to compensate the local surface charge imbalance and thus stabilize the crystal surfaces. Therefore, AgBr nanoplates exposed with {111} facets can be produced by preferential adsorption of PVP during the crystal growth process [34]. Benefiting from the high activity of {111} facets, both of AgBr tetrakaidecahedrons and nanoplates show much higher photocatalytic activity for the degradation of MO dye than the irregular AgBr particles. For instance, the photodegradation rate Of MO over Ag/AgBr tetrakaidecahedron is at least four times faster than that of irregular AgBr microstructures, as well as 20 times higher than the highly efficient Ag$_3$PO$_4$ photocatalyst [34].

Huang's group [35] synthesized AgCl concave cubes with highly active facets via wet chemical oxidization method using NaClO$_2$ as an oxidizer to tune the supply of Ag$^+$ during the growth process of AgCl cubic seeds, together with Cl$^-$ as capping reagent (Fig. 5). The growth process of AgCl microcrystals is summarized in Scheme 3. Firstly, under acidic conditions, ClO$_2^-$ ions react with Ag plate to generate Ag$^+$ ions which further react with Cl$^-$ ions to form cubic AgCl seeds. Because the concentration of Ag$^+$ ions is far lower than that of Cl$^-$, the excess Cl$^-$ ions absorb on the surface of cubic AgCl seeds. For a cubic seed, the reactivity of different sites is supposed to decrease in the order of corners, edges, and side faces. Therefore, the cubic seeds grow faster along (111) and (110) directions than along the (100) direction. As a result, the concave cubes can be obtained by preferential overgrowth along (111) and (110) directions. At higher NaCl concentration, AgCl crystals grow only along (111) directions to form flower-like structures. The result of O$_2$ evolution indicated that AgCl concave cubes with highly active facets show higher photocatalytic activity than the flat {001} enclosed cubes, which is because highly active facets have large numbers of atomic steps, edges and kinks.

By an ionic liquids (ILs)-assisted hydrothermal method, Huang's group prepared a series of AgCl and AgBr microcrystals [90, 91]. They systematically investigated the influence of the length of ILs' alkyl chain on the morphology and exposed crystal facets of the obtained AgCl and AgBr micro-crystals. When 3-methylimidazolium chlorides (C$_x$MimCl, $x = 4, 8, 12, 16$) were employed as

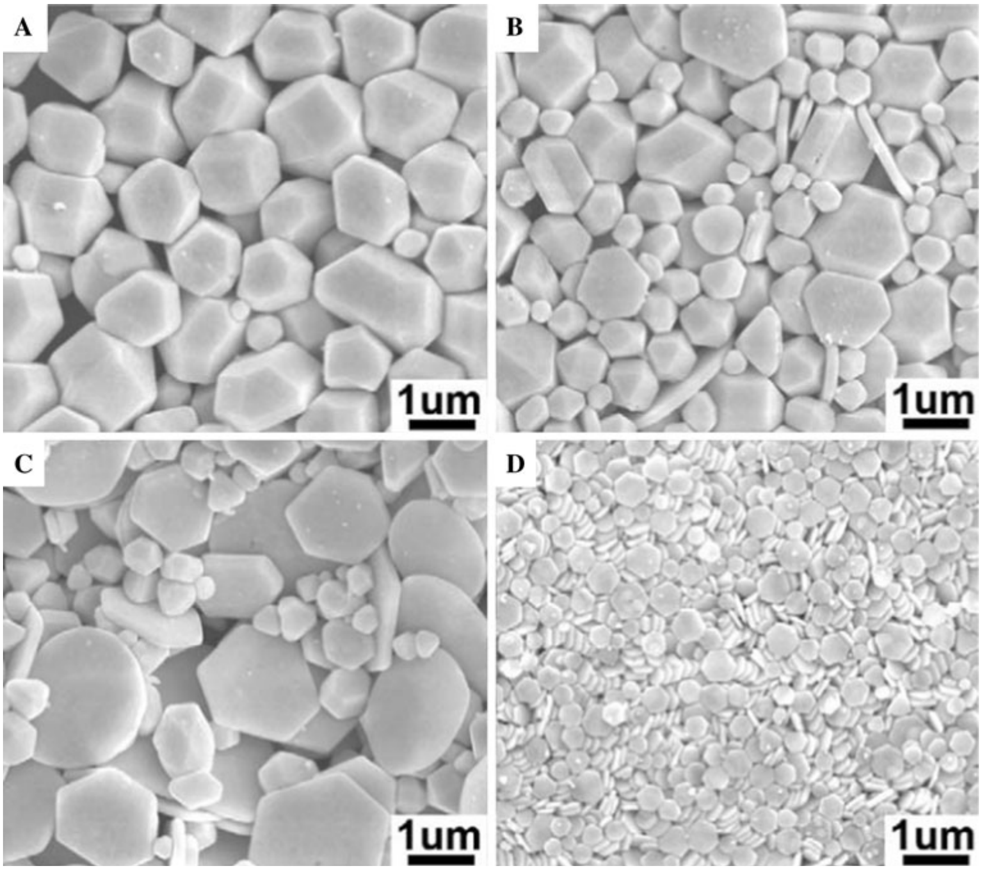

Fig. 4 SEM images of as-prepared AgBr nanoparticles produced with the different molar ratio of PVP to $AgNO_3$: **a** 6.7, **b** 13.4, **c** 40.2 and **d** 67 [34]

capping agent, the morphlogy of AgCl microcrystals evolved gradually from cubes with sharp edges in the absence of C_xMimCl to near microspheres in the presence of C_{16}MimCl. The formation mechanisms of different morphologies are schematically illustrated in Fig. 6. According to Charles Frank's kinematic theory of crystal growth, steps are firstly generated with the face growth rate (V) perpendicular to the crystal facets, followed by the growth with step velocity (R) parallel to the crystal facets, and microcosmic steps are formed on the surface of the crystal (Fig. 6c). In absence of C_xMimCl, the step growth velocity R is high and new steps can rapidly grow across the crystal facet and planar faces are formed. Therefore, AgCl crystal nuclei can gradually grow into cubic microcrystals by Ostwald ripening process (Fig. 6a). When C_xMimCl is present, C_xMim$^+$ ions adsorbed on the surface of AgCl nuclei will restrict the diffusion of Ag^+ to form AgCl and slow down the step growth velocity R, leading to the formation of a series of microcosmic steps (Fig. 6b). These microcosmic steps form the convex faces of near-spherical AgCl microcrystals.

When C_4MimBr was used as capping agent, AgBr microcrystals with exposed {110}, {101}, and {011} facets are produced, as shown in Fig. 7. Normally, {100} facets are easily exposed because the surface energy of {100} facets is lower than that of {111} and {110} facets. However, after adsorbing C_4MimCl, the surface energies of {110}, {101}, and {110} facets decrease more significantly than that of {001} facets, resulting in the formation of {110}, {101}, and {110} facets. With the further increase of alkyl chain's length, the apophysis of {110}, {101}, and {011} facets becomes more and more apparent. Finally, near-spherical morphology can be produced when C_{16}MimBr is employed [91].

Photocatalytic degradations of MO and RhB dyes indicated that near-spherical AgCl and AgBr microcrystals exhibit the highest photocatalytic activity compared to their cubic and other morphological counterparts. The obtained excellent photocatalytic performance is probably because the near-spherical surface contained a series of highly active facets [90, 91].

2.4 Spherical Ag/AgBr Photocatalysts

Geng et al. [32] fabricated AgBr microspheres with diameter ranging from 0.6 to 1.2 μm by a facile hydrothermal process

Fig. 5 SEM images of AgCl samples prepared at different reaction time: **A** 0.5 h, **B** 1 h, **C** 4 h, **D** 8 h in 2 mM $NaClO_2$ and 0.80 mM NaCl; and at different concentrations of NaCl solution: 0.78 mM (**a**), 1.00 mM (**b**), 1.37 mM, (**c**) and 1.97 mM (**d**) for 1 h in 2 mM $NaClO_2$. *Scale bar* 300 nm [35]

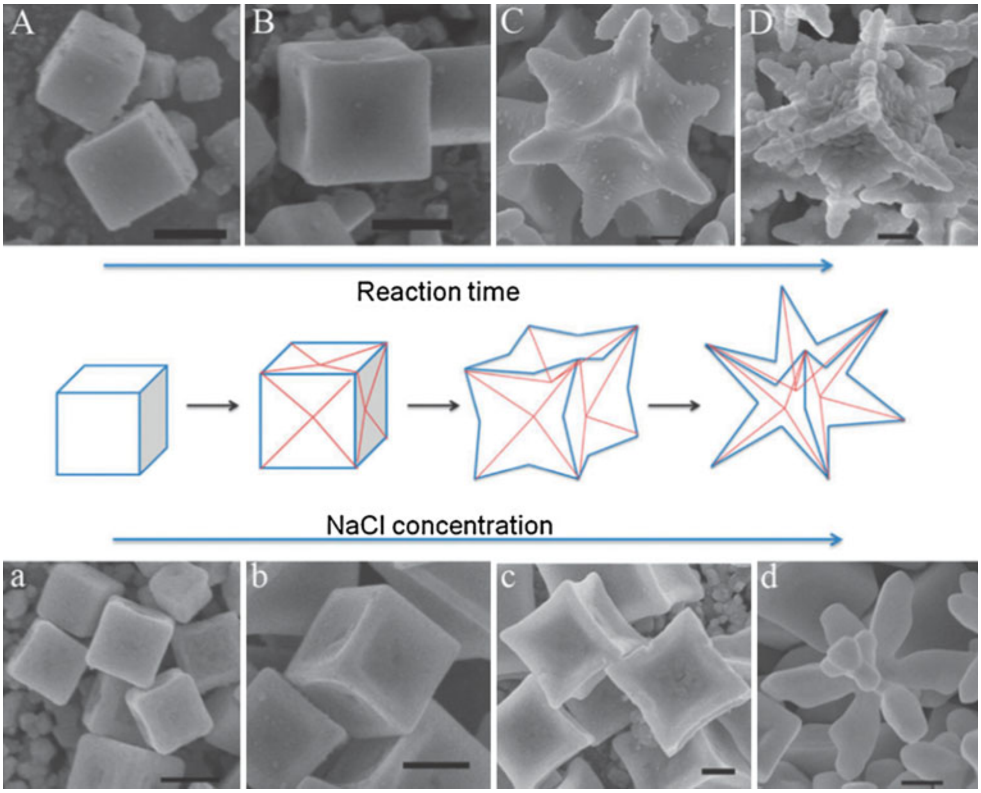

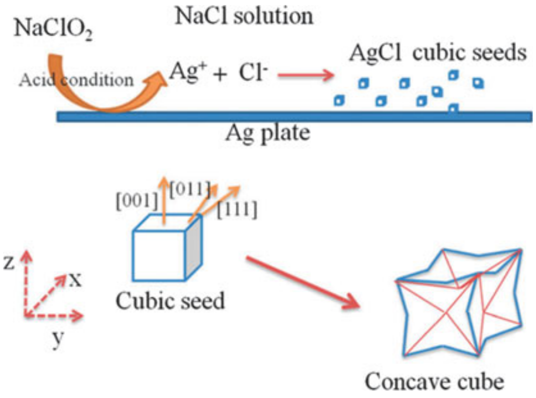

Scheme 3 Growth mechanism of concave AgCl [35]

(120 °C, 6 h) in the presence of hexadecyltrimethylammonium bromide (CTAB) (Fig. 8). After sunlight irradiation, the Ag nanoparticles with sizes of 8–12 nm can be anchored on the surface of AgBr microspheres. The result of degrading MO dyes indicated that the as-prepared Ag/AgBr photocatalyst exhibited excellent visible light photocatalytic activity and recycling stability. Using a multi-amine head surfactant $C_{18}N_3$ as a soft template, Jiang et al. [92] fabricated Ag/AgCl hollow spheres by adding $AgNO_3$ to micelles of $C_{18}N_3$ dispersed in HCl solution. The diameter of Ag/AgCl hollow spheres can be tuned in the range of 100 nm to 1200 nm by adjusting the aging time. The concentration of $C_{18}N_3$ plays a key role in determining the morphology of the product. When the $C_{18}N_3$ concentration was 3 mmol L^{-1}, the ruptured nanoparticles were obtained along with the integrated Ag/AgCl hollow spheres (Fig. 9a). When the $C_{18}N_3$ concentration was higher than 5 mmol L^{-1}, the hollow spheres became rigid and stable (Fig. 9b). However, the hollow spheres would interconnect and agglomerate when the concentration reached approximately 50 mmol L^{-1} (Fig. 9c). Yang et al. [93] prepared AgI hollow spheres with an average radius of 100–200 nm by a simple reaction between AgBr suspension and KI in the presence of gelatine. Gelatin was found to play a decisive role in the formation of AgI hollow microspheres.

2.5 Porous Ag/AgX Photocatalysts

It is well known that photocatalytic reaction is a surface-based reaction, thus a large surface area is usually beneficial for the photocatalytic reaction because it can supply more adsorption sites and photocatalytic reaction centers [94]. By dealloying AgAl alloys with NaOH solution and a subsequent surface chlorination in H_2O_2 and HCl mixed solution, Ding et al. [33] fabricated porous AgCl/Ag composite nanostructure that inherited the bicontinuous spongy morphology of nanoporous silver precursor with interconnected pore channels and solid ligaments (Fig. 10). The existence of Ag in the structure was found to contribute greatly to enhanced absorption in the visible light

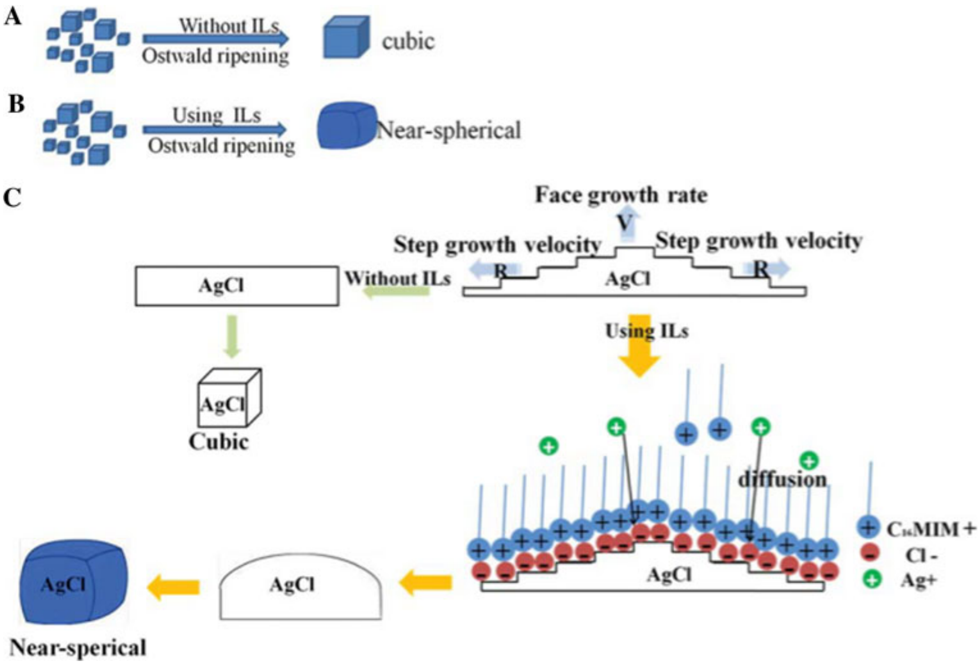

Fig. 6 **a** The growth process of AgCl without ionic liquids. **b** The growth process of AgCl using ionic liquids as stabilizer. **c** The formation mechanism of planar and convex faces of near-spherical AgCl [90]

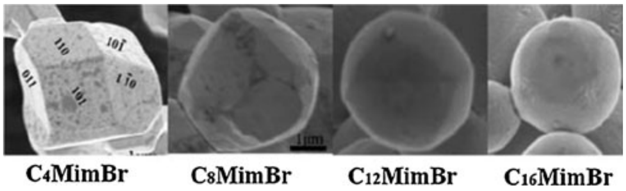

Fig. 7 SEM images of AgBr microcrystals synthesized with C_4MimBr, C_8MimBr, C_{12}MimBr, and C_{16}MimBr, respectively [91]

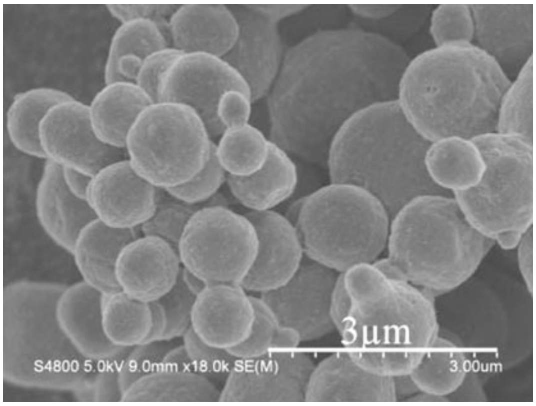

Fig. 8 SEM images of the as-prepared Ag/AgBr before photocatalytic reaction [32]

region, while the interconnected pore channels not only provide more photoactive sites but also favor the transportation of reactants and degradation products. The photocatalytic degradation of MO dye under visible light irradiation indicated that porous AgCl/Ag composite photocatalyst exhited much higher photocatalytic activity when compared with bulk AgCl and squeezed porous AgCl/Ag catalysts. Yang et al. [95] prepared AgBr porous spheres with an average diameter of 150–200 nm by a simple reaction between AgCl suspension and KBr in the presence of gelatin (Fig. 11). It was found that gelatin played a decisive role in inhibiting the coagulation of AgBr porous spheres.

2.6 Other Morphologies

Huang's group [96] synthesized Ag/AgCl plasmonic photocatalysts with various morphological structures including microrods, the mixture of microrods and irregular spheres, and hollow spheres by following procedures: Firstly, silver molybdate precursors with rod-, cubic- and polyhedron-like shapes were prepared by adjusting the acidity of microwave-assisted hydrothermal system (Fig. 12a–c). Secondly, ion-exchange process between the silver molybdate precursors and hydrochloric acid was employed to produce AgCl counterparts with different morphologies. Finally, Ag/AgCl plasmonic photocatalysts with various morphological structures were produced by a light-induced chemical reduction reaction (Fig. 12d–f). The influences of morphological structures on the photocatalytic performance of Ag/AgCl photocatalysts were evaluated by measuring the decomposition of MO dye under visible-light irradiation ($\lambda \geq 400$ nm). As shown in Fig. 13, hollow spheres (sample c) exhibit higher photocatalytic activity than microrods (samples a) and the mixture of microrods and irregular spheres (sample b). During the MO degradation process, the MO molecules can

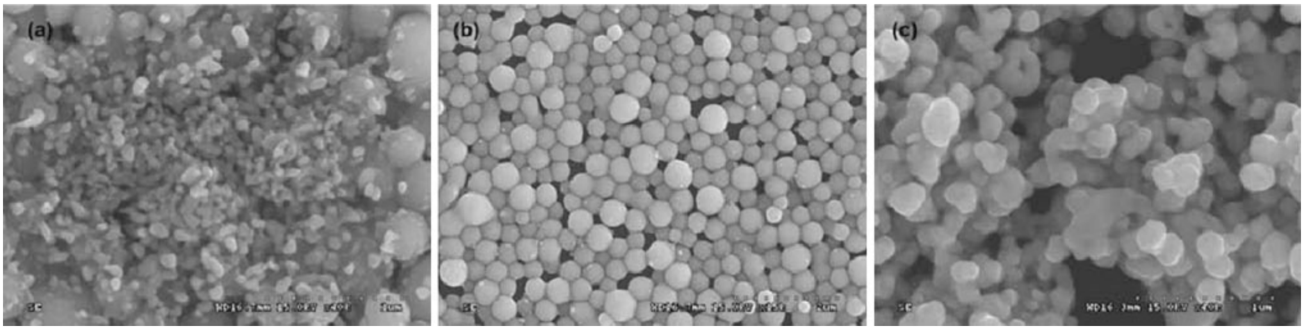

Fig. 9 SEM images of the Ag/AgCl hollow spheres fabricated with $C_{18}N_3$ concentration at **a** 3 mmol L^{-1}, **b** 5 mmol L^{-1}, and **c** 50 mmol L^{-1}

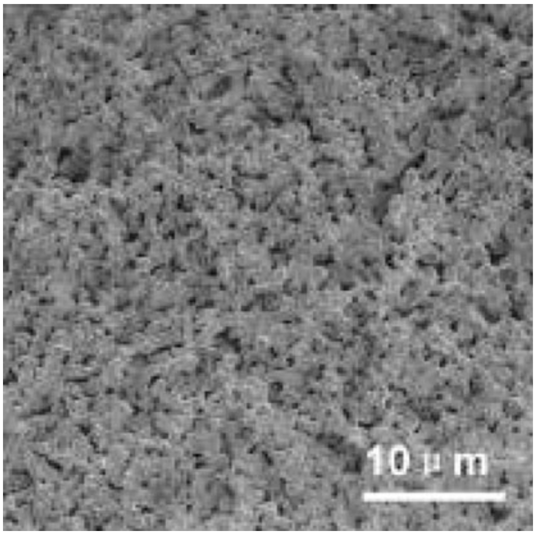

Fig. 10 SEM images of the porous AgCl/Ag nanocomposites [33]

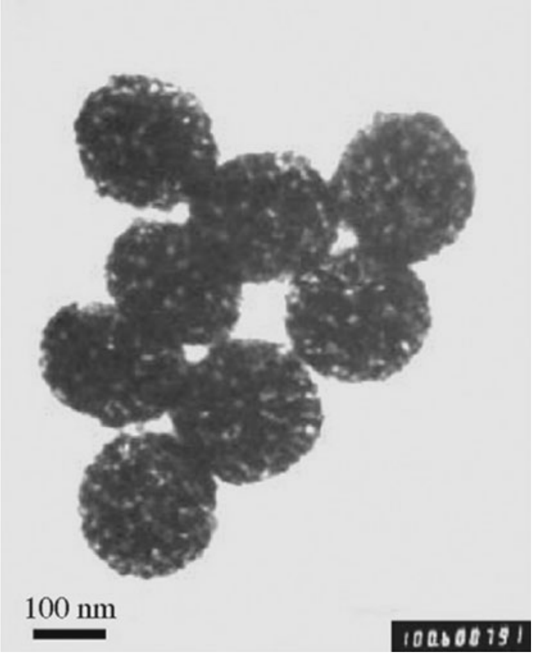

Fig. 11 TEM micrographs showing the spheres of AgBr prepared under the temperature of the reaction at 10 °C [95]

infiltrate the inside of the Ag/AgCl hierarchical hollow spheres, thus making contact with the inner and outer surface of hollow spheres, and hence improving the photocatalytic activity. As for the microrods, and the mixture of microrods and irregular spheres, the MO molecules can only contact with their outer surface, leading to inferior photocatalytic activity.

An et al. [96] synthesized heterostructured Ag/AgBr/AgCl nanocashews by an anion-exchange reaction between AgCl nanocubes and Br^{-1} ions, followed by photoreduction (Fig. 14). Compared to polyhedral Ag/AgBr nanoparticles, the obtained nanostructures exhibited enhanced photocatalytic activity towards the decomposition of organic pollutant rhodamine-B. Interestingly, the novel heterostructured Ag/AgBr/AgCl nanophotocatalyst also showed efficient visible light conversion of CO_2 to energetic fuels, e.g. methanol/ethanol. The as-prepared photocatalyst exhibited a relatively strong adsorption for organic molecules, which is beneficial to the improvement of photocatalytic activity.

By ripening of AgCl nanoparticles in ethylene glycol solution containing PVP as capping molecules, Sun et al. [97] AgCl microcrystals with cube-tetrapod morphology and narrow particle size distribution (Fig. 15). The obtained cube-tetrapod AgCl nanoparticles can efficiently photodecomposition of methylene blue under white light illumination.

3 Photocatalytic Mechanism and Applications

Until now, AgX-based photocatalytic materials have been successfully used in the fields of organic pollutant degradation, H_2 or O_2 production, NO_x conversion, CO_2 reduction, and disinfection, as summarized in Table 1 [10, 11, 13, 16, 19, 21, 24, 29, 62, 67, 68, 89–91, 96–119]. Here, we mainly discuss the photocatalytic mechanism and

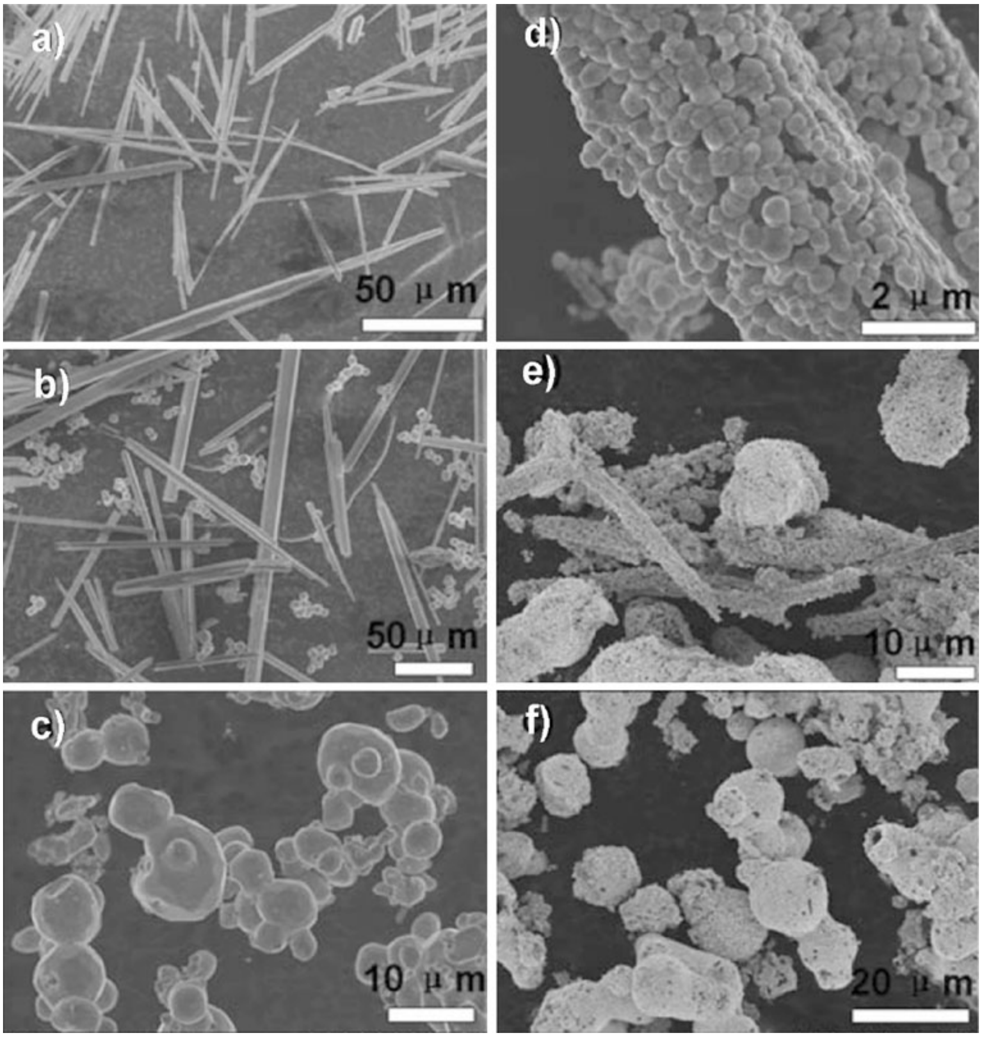

Fig. 12 SEM images of **a** $Ag_{1.028}H_{1.852}Mo_{5.52}O_{18}$ microrod, **b** Ag_2MoO_4 microrods and cubes, **c** polyhedron-like Ag_2MoO_4, **d** Ag/AgCl microrods, **e** Ag/AgCl microrods and irregular spheres, **f** Ag/AgCl hollow spheres. The pictures were rearranged according to Ref. [96]

applications of AgX (Ag/AgX) and some supported AgX photocatalysts.

3.1 Photocatalytic Mechanism of AgX (Ag/AgX) Photocatalysts

Semicondutor phothocatalytic reactions include four basic processes, i.e., charge carrier generation, charge trapping, charge recombination, and interfacial charge transfer [120, 121], which are severly enslaved to the type and microstructure of photocatalysts. For the AgX (X = Cl, Br, and I) photocatalytic materials, it is commonly accepted that metallic Ag will be produced on the surface of AgX after light irradiation [10, 15, 17, 24, 25]. However, there are some different understandings about the roles of Ag and AgX in the photocatalytic reactions. In the early studies, it was accepted that AgX is the active component responsible for light absorption and metallic Ag plays the role of separating photogenerated electrons and holes [10, 15, 17]. Moreover, it was also confirmed that the present of Ag is contributing to the photostability of AgX by scavenging holes and trapping electrons [15]. Several studies reported the excellent visible light activity of AgBr for organic pollutant degradation and bacteria inactivation [15, 17, 18]. Unfortunately, the role of metallic Ag as visible light sensitizer seems to be ignored. In 2008, Huang's group found that Ag/AgCl exhibited excellent photocatalytic activity for the degradation of methyl orange under visible light irradiation [24]. Pure AgCl can only absorb UV light because its direct and indirect bandgaps are 5.6 and 3.25 eV, respectively [24]. Therefore, the high photocatalytic activity under visible light irradiation should be ascribed to the contribution of Ag nanoparticles, which can absorb visble light by surface plasmon resonance (Fig. 16).

When a metal particle is exposed to light, the oscillating electromagnetic field of the light induces a collective

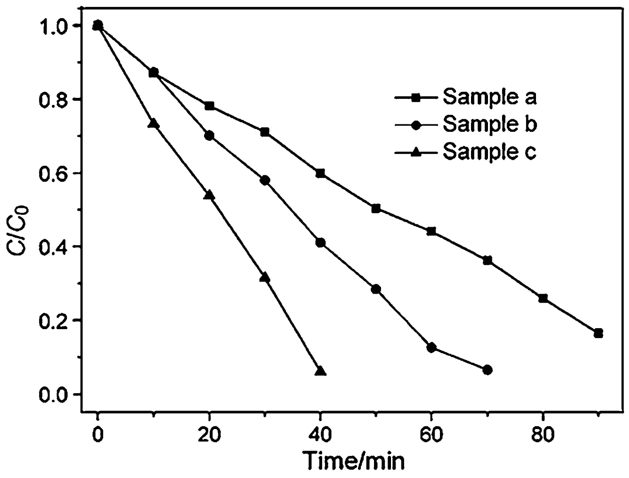

Fig. 13 Photodecomposition of MO dye in solution (20 mg L^{-1}) over Ag/AgCl (samples *a–c*) under visible-light irradiation (≥400 nm). *C* is the concentration of MO at time *t*, and C_0 is the concentration of MO after adsorption–desorption equilibrium in the dark [96]

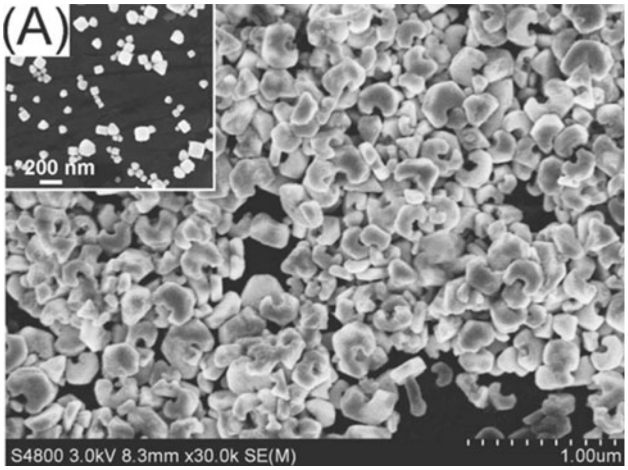

Fig. 14 SEM images of the as-prepared Ag/AgBr/AgCl and (*inset*) AgCl

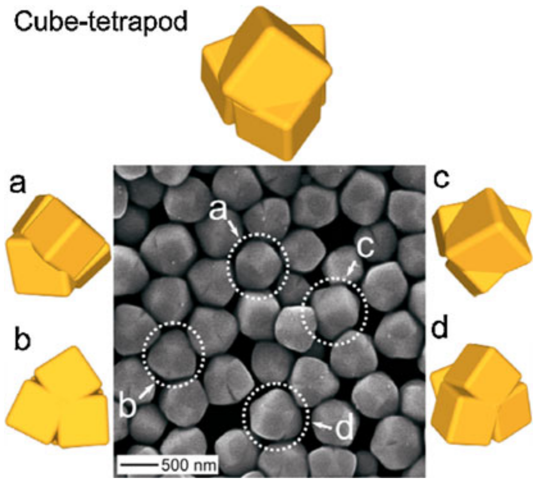

Fig. 15 Schematic drawings and SEM image of the cube-tetrapod nanoparticles

coherent oscillation of the free electrons of the metal. This electron oscillation around the particle surface causes a charge separation with respect to the ionic lattice, forming a dipole oscillation along the direction of the electric field of the light (Fig. 17) [122]. The amplitude of the oscillation reaches maximum at a specific frequency, called surface plasmon resonance (SPR) [123]. For noble metals, especially as Au and Ag, the SPR band is much stronger than other metals. The SPR band intensity and wavelength depends on the factors such as the metal type, particle size, shape, structure, composition and the dielectric constant of the surrounding medium [124].

The photocatalytic performance of a semiconductor photocatalyst can be effectively enhanced by SPR effect [125–129]. It is speculated that the metallic SPR enhances the photocatalytic activity of nearby semiconductors by transferring energy to the semiconductor and increasing the steady-state concentration of 'chemically useful' energetic charge carriers in the semiconductor [124]. There are three non-mutually exclusive energy-transfer mechanisms by which SPR can enhance the concentration of charge carriers, e.g., SPR-mediated charge injection from metal to semiconductor, Near-field electromagnetic, and scattering mechanisms [124]. For the Ag/AgX plasmonic photocatalysts, the in situ formed Ag nanostructures by chemical or light reduction are in direct contact with its matrix AgX, allowing a rapid transfer of charge carriers from Ag nanoparticles to AgX. Therefore, the enhancement of visible light photocatalytic activity is probably realized by SPR-mediated charge injection from Ag to AgX.

AgBr has an indirect band gap of 2.6 eV [25], while AgI also has a narrow direct band gap (2.4 eV for α-AgI, 2.8 eV for β-AgI) [130]. Therefore, the Ag/AgBr and Ag/AgI can absorb visible light not only by Ag nanoparticles but also by their own intrinsic absorption.

3.2 Photocatalytic Degradation of Organic Pollutants

Figure 18 illustrates the degradation process of organic pollutants over Ag/AgX plasmonic photocatalysts, using AgCl as an example [101]. When Ag/AgCl is irradiated by visible light, Ag nanoparticles produce photo-generated electrons and holes, which can be separated by the SPR-induced local electromagnetic field [24]. Normally, AgCl is synthesized in chloride-riched condition, so the surface of AgCl is terminated by Cl^- ions and is therefore negatively charged. Due to the polarization effect of negatively charged AgCl surface, the electrons are transferred to the surface of Ag nanoparticles farthest away from the Ag/AgCl interface, while holes are transferred to the surface of

Table 1 Applications of silver halide photocatalys

Applications	Photocatalysts	Light source	Reference
Orgainic pollutant degradation			
MO	Ag/AgCl hybrid nanocubes	Visible light, $\lambda \geq 400$ nm	[31]
	AgCl nanocubes	Sunlight	[21]
	Cube-like Ag/AgCl	500 W Xe lamp, $\lambda \geq 400$ nm	[68]
	Quasi-cubic Ag/AgCl	Sunlight or visible light	[30]
	Ag/AgCl core–shell nanowires	300 W Xe lamp, $\lambda \geq 420$ nm	[26]
	AgBr Nanowires	300 W Xe lamp, $\lambda \geq 420$ nm	[27]
	Near-spherical AgCl crystal	300 W Xe arc, $\lambda \geq 400$ nm	[90]
	{111} Facet Exposed AgBr Microcrystals	300 W Xe lamp, $\lambda \geq 400$ nm	[89]
	AgBr nanoplates with exposed {111} facets	300 W Xe lamp, $\lambda \geq 400$ nm	[34]
	Ag/AgBr micrspheres	Sunlight	[32]
	Porous AgCl/Ag	300 W Xe, $\lambda \geq 420$ nm	[33]
	Ag/AgCl with different morphologies	300 W Xe, $\lambda \geq 400$ nm	[96]
	Ag/AgBr	300 W Xe, $\lambda \geq 400$ nm	[25]
	Ag/AgBr particles	36 W fluorescent lamps, $\lambda \geq 400$ nm	[29]
	Ag/AgBr	300 W halogen lamp, $\lambda \geq 400$ nm	[25]
	Ag/AgCl	300 W Xe, $\lambda \geq 400$ nm.	[24]
	Ag/AgBr	150 W tungsten halogen lamps	[98]
	Ag/Ag(Cl,Br), Ag/AgCl-AgI	300 W Xe, $\lambda \geq 400$ nm.	[99]
	AgCl/Ag	30 W daylight fluorescent lamp,	[100]
	Ag/AgCl	150 W tungsten halogen lamp, $\lambda > 400$ nm.	[101]
	Ag/AgCl coated PAN nanofibers	500 W Xe lamp, $\lambda \geq 420$ nm.	[102]
	AgBr/Y-zeolite	60 W halogen lamp	[103]
Acid Orange 7	AgBr carried by Fe_3O_4 magnetic particle	300 W Xe lamp, $\lambda \geq 400$ nm	[104]
RhB	Ag/AgCl hybrid nanocubes	Visible light, $\lambda \geq 400$ nm	[31]
	AgBr microcrystals with different morphologies	Xe lamp, $\lambda > 420$ nm	[91]
	Ag/AgBr/AgCl	300 W Xe, a UV cut-off filter	[96]
	AgCl/Ag	30 W daylight fluorescent lamp	[100]
	AgBr, AgBr/palygorskite	450 W Xe lamp, $\lambda \geq 400$ nm	[105]
	Fe_3O_4/SiO_2/AgCl/Ag	300 W Xe lamp with a UV-cutoff filter	[106]
	Ag–AgI/Fe_3O_4/SiO_2	250 W metal halide lamp, $\lambda \geq 420$ nm	[107]
MB	Ag/AgCl hybrid nanocubes	Visible light, $\lambda \geq 400$ nm	[31]
	Cube-like Ag/AgCl	150 W Quartz halogen lamp	[67]
	AgCl Nanowires Decorated with Auparticles	150 W Quartz halogen lamp	[62]
	AgCl cube-tetrapod morphology	300 W halogen lamp, $\lambda \geq 400$ nm	[97]
	AgCl/Ag/MCM-41	200 W tungsten filament lamp, $\lambda \geq 400$ nm	[108]
	AgBr/nanoAlMCM-41	A 200 W tungsten filament Philips lamp	[109]
Isopropyl alcohol	AgBr/Ag	300 W halogen lamp, $\lambda \geq 400$ nm	[25]
2-Chlorophenol	Ag/AgCl/Cotton-fabric	250 W metal halide lamps	[110]
	Ag/AgBr/Al_2O_3	350 W Xe lamp, $\lambda \geq 420$ nm	[111]
	Ag/AgI/Al_2O_3	350 W Xe lamp, $\lambda \geq 450$ nm	[19]
4-chlorophenol	Ag–AgI/Fe_3O_4/SiO_2	250 W metal halide lamp, $\lambda \geq 420$ nm	[107]
2,4-dichlorophenol	Ag/AgBr/Al_2O_3	350 W Xe lamp, $\lambda \geq 420$ nm	[111]
	Ag/AgI/Al_2O_3	350 W Xe lamp, $\lambda \geq 450$ nm	[19]
Trichlorophenol	Ag/AgBr/Al_2O_3	350 W Xe lamp, $\lambda \geq 420$ nm	[111]
	Ag/AgI/Al_2O_3	350 W Xe lamp, $\lambda \geq 450$ nm	[19]
Pentachlorophenol	AgCl/Ag	30 W daylight fluorescent lamp	[100]
p-nitrophenol	Ag–AgBr/Al_2O_3	300 W Xe lamp, $\lambda \geq 400$ nm	[112]

Table 1 continued

Applications	Photocatalysts	Light source	Reference
CH_3CHO	AgBr/Al-MCM-41	1000 W high-pressure mercury lamp, $\lambda \geq 420$ nm	[16]
H_2 evolution	$AgBr/SiO_2$	100 W high-pressure Hg lamp	[10]
O_2 evolution	AgCl concave cubes	300 W Xe lamp (UV/vis and vis light)	[35]
	AgCl colloids	Xe lamp, $\lambda \geq 300$ nm	[113]
	AgCl-coated electrode	200 W mercury lamp	[114]
	AgCl electrode	450 W Xe lamp	[11]
	AgCl/Zeolite	450 W Xe lamp	[115]
	AgCl-coated electrodes	450 W Xe lamp	[116]
CO_2 reduction	Ag/AgBr/AgCl	300 W Xe lamp, $\lambda \geq 420$ nm	[96]
	AgBr, AgBr/palygorskite	450 W Xe lamp, $\lambda \geq 400$ nm	[105]
NO_x conversion	$AgCl/Al_2O_3$	500 W Xe lamp	[13]
Cr^{6+} reduction	Ag/Ag(Cl,Br), Ag/AgCl-AgI	300 W Xe lamp, $\lambda \geq 400$ nm	[99]
Disinfection			
Escherichia Coli	$Ag-AgI/Al_2O_3$	350 W Xe lamp, $\lambda \geq 420$ nm	[117]
Shigella dysenteriae, human rotavirus type 2	$Ag-AgI/Al_2O_3$	350 W Xe lamp, $\lambda \geq 420$ nm	[117]
Gram-positive, gram-negative bacteria	$AgBr/TiO_2$	350 W Xe lamp, $\lambda \geq 420$ nm	[118]

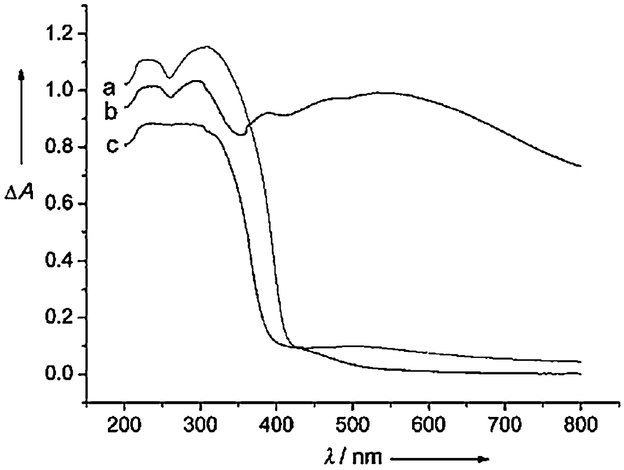

Fig. 16 UV–Vis diffuse-reflectance spectra of (*a*) AgCl, (*b*) Ag@AgCl, and (*c*) N-doped TiO_2 [24]

AgCl. Subsequently, the electrons will be further trapped by adsorbed O_2 to form $^{\bullet}O_2^-$ and other reactive oxygen species. Meanwhile, the holes will combine with Cl^- ions to form Cl^0 atoms. Because of the high oxidation ability of the Cl^0 atoms, the MO dye could be oxidized by the chlorine atoms and hence the Cl^0 could be reduced to chloride ions again [24]. So, the Ag/AgCl plasmonic photocatalysts can remain stable without deterioration.

For the Ag/AgBr photocatalyst, both Ag nanoparticles and AgBr can response to visible light, which can produce more electrons and holes [32]. Therefore, Ag/AgBr usually shows higher photocatalytic activity than Ag/AgCl [25].

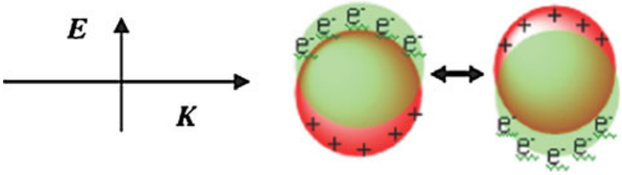

Fig. 17 Schematic illustration of surface plasmon resonance in plasmonic nanoparticles [121]

However, Huang et al. [24] think that there are three steps involving the photocatalytic reaction of Ag/AgX (X = Cl, Br): (1) the light-absorption to generate electrons and holes, (2) the combination of a photo-generated hole with X^{-1} to form X^0, and (3) the oxidation by X^0. The electron affinity of Br^0 (324 kJ mol^{-1}) is lower than that of Cl^0 (349 kJ mol^{-1}), which makes it easier for Br^- than for Cl^{-1} to combine with a hole. Thus, the rate-determining step of the photocatalytic reaction is the step in which a hole combines with X^- to form X^0. Therefore, Ag/AgBr shows higher photocatalytic activity than Ag/AgCl.

Some researchers advanced a different viewpoint about the photocatalytic mechanism of Ag/AgX plasmonic photocatalysts, which mainly involves in the transfer pathway of electrons and holes as well as the presence/or absence of superoxide anion radicals [10, 11]. For instance, Zhang et al. [10, 11] think that the electrons formed on Ag/AgBr plasmonic photocatalyst by SPR will transfer to the conductor band of AgBr because the work function of AgBr (5.3 eV) is higher than that of Ag (4.25 eV). They also suggest that photogenerated electrons cannot reduce O_2 to $^{\bullet}O_2^-$ through one-electron reaction

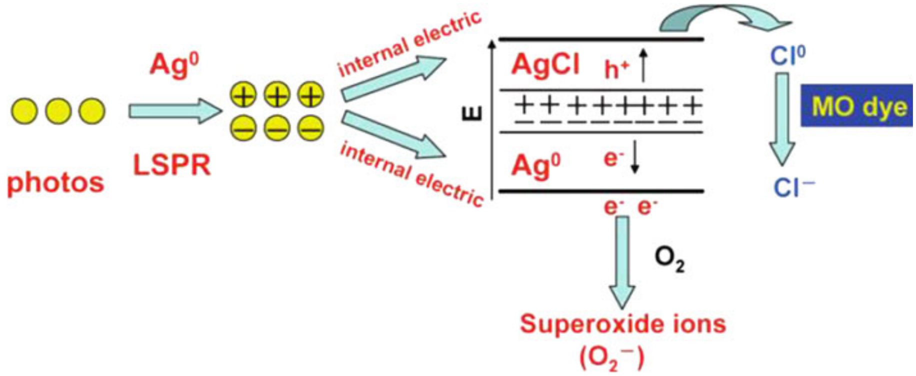

Fig. 18 Schematic model of the photocatalytic mechanism for Ag/AgCl [101]

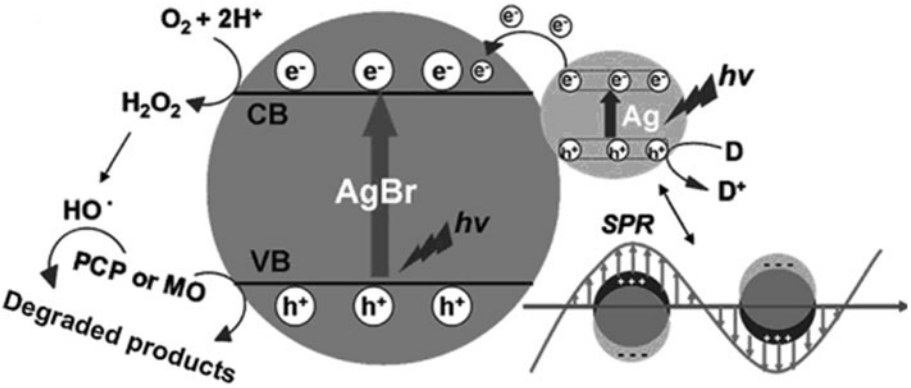

Fig. 19 Schematic illustration of the synergistic effect between AgBr and Ag NPs [10]

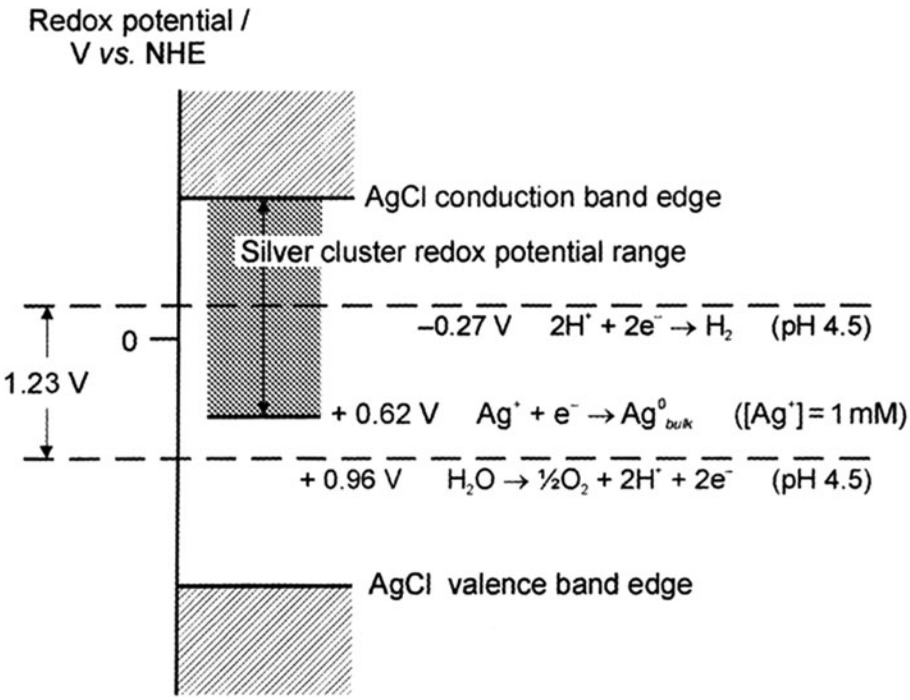

Fig. 20 Redox potentials for Ag^+/Ag^0_{bulk} at $[Ag^+] = 10^{-3}$ M, for the oxidation (O_2/H_2O) and reduction (H_2O/H_2) of water at pH 4.5, and position of the semiconductor band edges of AgCl. The band edges are approximately at +2.1 V (valence band) and −1.2 V (conduction band) vs. NHE. The electrochemical potential range of small silver cluster is indicated (shaded region) [114]

($O_2 + e^- \rightarrow {}^\bullet O_2^-$, $O_2/{}^\bullet O_2^-$: −0.33 eV vs. NHE), while $^\bullet$OH can be produced by the two-electron oxygen reduction route ($O_2 + 2H^+ + 2e^- \rightarrow H_2O_2 \rightarrow {}^\bullet OH$). h^+ and $^\bullet$OH serve as the main active species involved in the photodegradation of organic compounds in Ag/AgBr (Fig. 19).

3.3 O_2 and H_2 Generation

Figure 20 shows the redox potential range of reduced silver species with respect to thermodynamically required redox potentials for water oxidation and reduction at a pH value of 4.5. The redox potentials for electrochemical water oxidation and for water reduction are $E[O_2/H_2O] = +0.96$ V and $E[H_2O/H_2] = -0.27$ V (vs. NHE), and the thermodynamically required potential difference for water splitting is $\Delta E[H_2O \rightarrow H_2 + (1/2)O_2] = -1.23$ V [131]. The valence band edge and conduction band of AgCl are +2.1 and −1.2 V (vs. NHE), respectively. Therefore, photocatalytic generation of H_2 and O_2 by AgCl photocatalyst is allowable in energy levels.

The former studies have reported photochemical O_2 evolution in an aqueous AgCl suspension or colloids [131–136]. However, no way to the reoxidation of the reduced silver was given. Calzaferri et al. investigated the photochemical properties of systems containing AgCl and Ag^+-A zeolite [137–143]. These studies indicated that efficient photochemical oxidation of water to O_2 on AgCl takes place in the presence of a small excess of Ag^+ ions ($\sim 10^{-3}$ M), with a maximum evolution rate at pH 4–6. The mechanism for the photochemical water oxidation on AgCl is presented as follows [115]:

Firstly, electrons and holes are produced after AgCl absorbing light (Eq. 2). The electron hole-pairs may recombine (Eq. 3), or electrons and holes may separate and finally be trapped as reduced silver atoms $Ag^0_{s,i}$ (Eq. 4), or $Cl_s^\bullet$ radicals (Eq. 5). The indices s and i refer to surface and interstitial species.

$$AgCl \xrightarrow{hv} AgCl + h^+ + e^- \tag{2}$$

$$h^+ + e^- \rightarrow kT \tag{3}$$

$$Ag^+_{s,i} + e^- \rightarrow Ag^0_{s,i} \tag{4}$$

$$Cl_s^- + h^+ \rightarrow Cl_s^\bullet \tag{5}$$

Subsequently, the $Cl_s^\bullet$ radicals may recombine to form Cl_2 (Eq. 6). Under the applied conditions ($[Ag^+] \sim 10^{-3}$ M, pH ~ 4–6), the Cl_2 reacts with water to produce hypochlorous acid (Eq. 7). Finally, AgCl acts as a catalyst for the decomposition of hypochlorous acid to molecular oxygen, protons, and chloride ions (Eq. 8). The total reaction for photochemical oxidation of water to O_2 over AgCl is presented in Eq. 9.

$$2Cl_s^\bullet \rightarrow Cl_2 \tag{6}$$

$$Cl_2 + H_2O \leftrightarrow HOCl + H^+ + Cl^- \tag{7}$$

$$2HOCl \xrightarrow{Ag^+} O_2 + 2H^+ + 2Cl^- \tag{8}$$

Eq. 9 is the total reaction derived from Eqs. 2–8

$$H_2O + 2Ag + \xrightarrow{AgCl,hv} 2H^+ + \frac{1}{2}O_2 + 2Ag^0 \tag{9}$$

The efficiency of O_2 evolution is also relative to the morphology as well as exposed facets of AgX photocatalysts. For instance, Huang's group reported that AgCl concave cubes with exposed highly active facets show higher activity for O_2 evolution [35].

Kakuta et al. [10] investigated the properties of AgBr photocatalyst in splitting of water to H_2 generation. They found that AgBr dispersed on SiO_2 support can continuously produce H_2 for 200 h in CH_3OH solution (Fig. 21). X-ray diffraction indicated that AgBr was not destroyed under successive UV illumination. They thought that the formed Ag^0 species might act as the sites for the H_2 formation similar to Pt on Pt/TiO_2, and then further destruction of AgBr did not take place. The role of SiO_2 support was considered to enhance the adsorption of methanol and improve the dispersity of AgBr crystallites, both of which are favorable to H_2 generation.

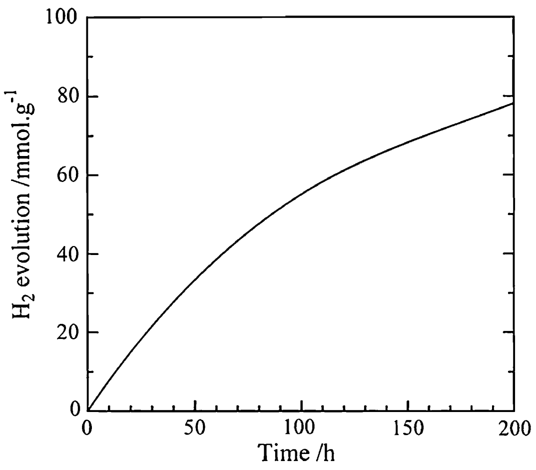

Fig. 21 Behavior of hydrogen evolution on $AgBr/SiO_2$ catalyst from CH_3OH/H_2O for 200 h [10]

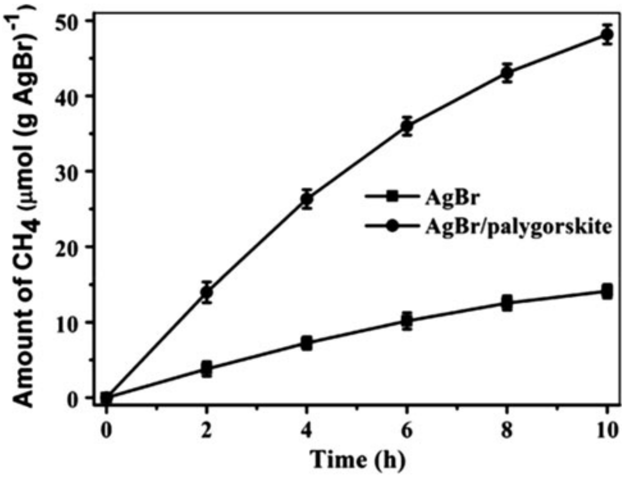

Fig. 22 Effect of palygorskite on photocatalytic performance of CO_2 reduction. *Error bars* represent standard deviations of triplicate measurements

3.4 CO_2 Reduction

Recycling of CO_2 to chemicals has been an increasingly important research topic due to its desirable role in alleviating fossil fuel depletion and the global warming problem. In recent years, semiconductor photcatalytic reduction of CO_2 to chemicals has received much research attention as an economic and environmentally friendly solution [8, 9, 144–146]. Zhang et at. [106] prepared AgBr/palygorskite composite and investigated the influence of palygorskite on photocatalytic performance of CO_2 reduction. It can be seen that palygorskite enhances the rate of CH_4 evolution by a factor of 2, about 4.8 μmol $h^{-1}(gAgBr)^{-1}$ (Fig. 22). The promotion effect of palygorskite for CO_2 reduction could be ascribed to following three factors. Firstly, palygorskite can supply enough large interfaces due to its high specific surface area, which is favorable to forming more active sites. Secondly, the size of AgBr particles mixed with palygorskite is smaller compared with that of bare AgBr particles, which could suppress the recombination of electron–hole pairs as well as improve the redox ability of AgBr particle due to quantum size effect. Thirdly, the porous structure of palygorskite could facilitate the access of reactants to get to the active sites, reduce the reflection of light, and thus enhance the reactive efficiency.

A probable mechanism for the reduction of CO_2 to CH_4 with H_2 over AgBr/palygorskite is put forward as follows [106]:

(i) Excitation of AgBr (Eq. 10)

$$\mathrm{AgBr} + hv \rightarrow h^+ + e^- \tag{10}$$

(ii) Production of $^{\bullet}Br$ and Ag (Eqs. 11–13)

$$e^- + \mathrm{Ag}^+ \rightarrow \mathrm{Ag} \tag{11}$$

$$\mathrm{Ag} + hv \rightarrow h^+ + e^- \tag{12}$$

$$h^+ + \mathrm{Br}^- \rightarrow {}^{\bullet}\mathrm{Br} \tag{13}$$

(iii) Production of $^{\bullet}H$ (Eqs. 14, 15)

$${}^{\bullet}\mathrm{Br} + \mathrm{H_2(Ads.)} \rightarrow {}^{\bullet}\mathrm{H} + \mathrm{HBr} \tag{14}$$

$$h^+ + \mathrm{H_2(Ads.)} \rightarrow {}^{\bullet}\mathrm{H} + \mathrm{H}^+ \tag{15}$$

(iv) Reduction and hydrogenation of CO_2 as well as regeneration of Br^- (Eqs. 16–24)

$${}^{\bullet}\mathrm{H} + e^- + \mathrm{CO_2(Ads.)} \rightarrow \mathrm{HCOO}^- \tag{16}$$

$$\mathrm{HCOO}^- + \mathrm{HBr} \rightarrow \mathrm{HCOOH(Ads.)} + \mathrm{Br}^- \tag{17}$$

$$\mathrm{HCOOH(Ads.)} + {}^{\bullet}\mathrm{H} + e^- \rightarrow \mathrm{H_2C(OH)O}^- \tag{18}$$

$$\mathrm{H_2C(OH)O}^- + \mathrm{HBr} \rightarrow \mathrm{HCHO(Ads.)} + \mathrm{H_2O} + \mathrm{Br}^- \tag{19}$$

or

$$\mathrm{H_2C(OH)O}^- + \mathrm{HBr} \rightarrow \mathrm{H_2C(OH)_2(Ads.)} + \mathrm{Br}^- \tag{20}$$

$$\mathrm{HCHO(Ads.)} + {}^{\bullet}\mathrm{H} + e^- \rightarrow \mathrm{CH_3O}^- \tag{21}$$

$$\mathrm{H_2C(OH)_2(Ads.)} + {}^{\bullet}\mathrm{H} \rightarrow {}^{\bullet}\mathrm{CH_3} + \mathrm{H_2O} \tag{22}$$

$$\mathrm{CH_3O}^- + \mathrm{HBr} \rightarrow \mathrm{CH_3OH(Ads.)} + \mathrm{Br}^- \tag{23}$$

$$\mathrm{CH_3OH(Ads.)} + {}^{\bullet}\mathrm{H} \rightarrow {}^{\bullet}\mathrm{CH_3} + \mathrm{H_2O} \tag{24}$$

(v) Evolution of CH_4 (Eqs. 25–28)

$${}^{\bullet}\mathrm{CH_2} + {}^{\bullet}\mathrm{H} \rightarrow \mathrm{CH_4} \tag{25}$$

$${}^{\bullet}\mathrm{CH_2} + \mathrm{H_2} \rightarrow {}^{\bullet}\mathrm{CH_3} + {}^{\bullet}\mathrm{H} \tag{26}$$

$${}^{\bullet}\mathrm{CH_3} + \mathrm{H_2} \rightarrow \mathrm{CH_4} + {}^{\bullet}\mathrm{H} \tag{27}$$

$${}^{\bullet}\mathrm{CH_3} + {}^{\bullet}\mathrm{H} \rightarrow \mathrm{CH_4} \tag{28}$$

He et al. [147] investigated the photocatalytic reduction yield of CO_2 over AgBr/TiO_2 photocatalyst. It was found that 23.2 % AgBr/TiO_2 had relatively high reduction yields under visible-light irradiation for 5 h, with a methane yield of 128.56 μmol g^{-1}, methanol yield of 77.87 μmol g^{-1}, ethanol yield of 13.28 μmol g^{-1}, and CO yield of 32.14 μmol g^{-1}, respectively. The high photocatalytic activities of AgBr/TiO_2 for CO_2 reduction is attributed to its strong absorption in the visible-light region.

The possible reaction mechanism of CO_2 with H_2O on the AgBr/TiO_2 was proposed as follows [147]: The exited holes reacted with adsorbed water molecules on the catalyst surface to form $^{\bullet}OH$ radicals and H^+ (Eq. 30). Subsequently, the interaction of H^+ ions with the excited electrons led to the formation of $^{\bullet}H$ radicals (Eq. 31). Meanwhile, the charge transferred to the conduction band of TiO_2 reacted with CO_2 to form $^{\bullet}CO_2^-$ (Eq. 32). These radicals reacted with each other to produce CO (Eq. 3). At the same time, carbon radicals ($^{\bullet}C$) were formed from CO by successive reactions (Eqs. 34, 35), then $^{\bullet}CH_3$ radicals were formed (Eq. 36). The CH_3 radicals tend to react with protons to produce methane (Eq. 37), methanol (Eq. 38).

$$\mathrm{AgBr/TiO_2} + \text{visible light} \rightarrow e^- + h^+ \tag{29}$$

$$\mathrm{H_2O} + h^+ \rightarrow {}^{\bullet}\mathrm{OH} + \mathrm{H}^+ \tag{30}$$

$$\mathrm{H}^+ + e^- \rightarrow {}^{\bullet}\mathrm{H} \tag{31}$$

$$\mathrm{CO_2} + e^- \rightarrow {}^{\bullet}\mathrm{CO_2^-} \tag{32}$$

$${}^{\bullet}\mathrm{CO_2^-} + {}^{\bullet}\mathrm{H} \rightarrow \mathrm{CO} + \mathrm{OH}^- \tag{33}$$

$$\mathrm{CO} + e^- \rightarrow {}^{\bullet}\mathrm{CO}^- \tag{34}$$

$${}^{\bullet}\mathrm{CO}^- + {}^{\bullet}\mathrm{H} \rightarrow {}^{\bullet}\mathrm{C} + \mathrm{OH}^- \tag{35}$$

$${}^{\bullet}\mathrm{C} + \mathrm{H}^+ + e^- \rightarrow {}^{\bullet}\mathrm{CH_2} \rightarrow {}^{\bullet}\mathrm{CH_3} \tag{36}$$

$${}^{\bullet}\mathrm{CH_3} + \mathrm{H}^+ + e^- \rightarrow \mathrm{CH_4} \tag{37}$$

$${}^{\bullet}\mathrm{CH_3} + {}^{\bullet}\mathrm{OH} \rightarrow \mathrm{CH_3OH} \tag{38}$$

3.5 Photocatalytic Disinfection of Pathogenic Bacteria

Photocatalytic disinfection of pathogenic bacteria is another important application of AgX-based photocataltic materials. Hu et al. [15, 18, 121, 148, 149] systematically studied the bactericidal properties of $AgBr/TiO_2$ and AgI/TiO_2 in terms of Escherichia coli (*E. coli*), Staphylococcus aureus, Gram-negative bacterium, Gram-positive bacterium, and Staphylococcus aureus. Their experimental results indicated that both $AgBr/TiO_2$ and AgI/TiO_2 exhibit high bactericidal activity under visible light irradiation. The results of electron spin resonance and of radical scavengers indicated that reactive active oxygen species such as $HO_2^\bullet$, $^\bullet OH$, $^\bullet O^{2-}$, and H_2O_2 were involved in the decomposition of pathogenic bacteria. Moreover, it was found that the electrostatic force interaction of the bacteria with the catalyst is crucial for high bactericidal efficiency [15, 121, 148]. Recently, Hu et al. further investigated the plasmon-induced photocatalytic inactivation of enteric pathogenic microorganisms over $Ag{-}AgI/Al_2O_3$ photocatalyst [120]. The catalyst showed highly effective at killing *Shigella dysenteriae* (*S. dysenteriae*), *Escherichia coli* (*E. coli*), and human rotavirus type 2 Wa (HRV-Wa) under visible-light irradiation. It was found that the bactericidal efficiency of $Ag{-}AgI/Al_2O_3$ can be enhanced by anions such as OH^-, $HCO_3{}^-$ and $SO_4{}^{2-}$ ions. The plasmon-induced h^+ on Ag NPs, $O_2^{\bullet -}$, and anionic radicals were involved in the bactericidal reaction.

Very recently, Hou et al. [150] investigated the mechanism of *E. coli* inactivation on $Ag/AgBr/TiO_2$ nanotube array electrode under visible light irradiation. The prepared composite electrode showed high activity for *E. coli* inactivation. The results revealed that oxidative attack from the exterior to the interior of the *Escherichia coli* by $OH^\bullet$, $O_2^{\bullet -}$, holes and Br^0, causing the cell to die.

The mechanisms of bactericidal reaction over the Ag/$AgBr/TiO_2{-}NA$ system are proposed as follows: Due to the dipolar character of the SPR of Ag nanoparticles, the photogenerated electrons from the plasmon-excited Ag nanoparticles (Eq. 39) transfer to the surface of the TiO_2 nanotubes farthest away from the Ag/AgBr interface (Eq. 40). Simultaneously, the leftover holes diffuse to the surface of the AgBr particles and cause the oxidation of Br^- ions to Br^0 atoms (Eq. 41). On the other hand, AgBr could be excited by visible light and generated electron–hole pairs (Eq. 42). Metallic Ag on the surface of the $Ag/AgBr/TiO_2$–NA traps photogenerated electrons (Eq. 43) and subsequent transfers the trapped electrons to the TiO_2 conduction band (Eq. 44). Some of the photogenerated holes could combine with Br^- to form Br^0 atoms which can kill *E. coli* and come back to Br^- again (Eq. 45). Whereas the other holes accumulated in AgBr could directly react with E. coli or interact with surface-bound H_2O or OH^- to produce the $OH^\bullet$ radicals (Eqs. 46, 47). Meanwhile, the photogenerated electrons at the surface of the TiO_2 could travel along the TiO_2 nanotubes, passed through the interface between TiO_2 and Ti to the external circuit under the external electric field (Eq. 48). Furthermore, photoelectrons arrived at the counter electrode surface could react with the adsorbed molecular oxygen to yield $^\bullet O_2{}^-$ (Eq. 49). The generated $^\bullet O_2{}^-$ then further combine with H^+ to produce $HO_2^\bullet$ (Eq. 50), which could react with the trapped electrons to generate $OH^\bullet$ radicals (Eq. 51). The reactive species such as Br^0, $OH^\bullet$, $^\bullet O_2{}^-$ and h^+, could attack the cell membrane and wall, causing bacteria to die (Eq. 52). The relevant reactions are expressed as follows [150]:

$$\mathrm{Ag} + \mathrm{hv} \rightarrow \mathrm{Ag}* \tag{39}$$

$$\mathrm{Ag} * + \mathrm{TiO_2} \rightarrow \mathrm{Ag}^{+\bullet} + \mathrm{TiO_2(e^-)} \tag{40}$$

$$\mathrm{Ag}^{+\bullet} + \mathrm{Br}^- \rightarrow \mathrm{Ag} + \mathrm{Br}^0 \tag{41}$$

$$\mathrm{AgBr} + \mathrm{hv} \rightarrow \mathrm{AgBr}(\mathrm{e}^- + \mathrm{h}^+) \rightarrow \mathrm{AgBr} + \mathrm{heat} \tag{42}$$

$$\mathrm{AgBr(e^-)} + \mathrm{Ag} \rightarrow \mathrm{AgBr} + \mathrm{Ag(e^-)} \tag{43}$$

$$\mathrm{Ag(e^-)} + \mathrm{TiO_2} \rightarrow \mathrm{TiO_2(e^-)} + \mathrm{Ag} \tag{44}$$

$$\mathrm{AgBr(h^+)} + \mathrm{Br}^- \rightarrow \mathrm{AgBr} + \mathrm{Br}^0 \tag{45}$$

$$\mathrm{AgBr(h^+)} + \mathrm{H_2O} \rightarrow \mathrm{H}^+ + {}^\bullet\mathrm{OH} \tag{46}$$

$$\mathrm{AgBr(h^+)} + \mathrm{OH}^- \rightarrow {}^\bullet\mathrm{OH} \tag{47}$$

$$\mathrm{TiO_2(e^-)} + \text{external eletrostatic field} \rightarrow \text{external circuit} \tag{48}$$

$$\text{Counter eletrode}(\mathrm{e}^-) + \mathrm{O_2} \rightarrow {}^\bullet\mathrm{O_2^-} \tag{49}$$

$$^\bullet\mathrm{O_2^-} + \mathrm{H}+ \rightarrow \mathrm{HO_2}^\bullet \tag{50}$$

$$2\mathrm{e}^- + \mathrm{HO_2}^\bullet + \mathrm{H}+ \rightarrow {}^\bullet\mathrm{OH} + \mathrm{OH}^- \tag{51}$$

$$\mathrm{Br}^0, {}^\bullet\mathrm{OH}, {}^\bullet\mathrm{O_2^-}, \mathrm{h}^+ + E.\,coli \rightarrow \text{inactivated } E.coli + \mathrm{Br}^- \tag{52}$$

4 Conclusion

In recent years, silver halide (AgX)-based photocatalytic materials have received increasing research attention owing to its excellent visible light-driven photocatalytic performances in the applications of organic pollutant degradation, H_2/O_2 generation, and disinfection. Experiments confirmed that the photocatalytic performances of AgX photocatalysts are severely dependent on their morphological structures. In the review, we mainly discussed the synthetic techniques, formation mechanism, and photocatalytic performances of different morphological AgX (Ag/AgX) materials such as nanowires, nano-/microcubes, micropheres, and highly active facet-exposed microcrystals. Ag/AgX core–shell nanowires can be fabricated by Ag-engaged galvanic replacement method using Ag nanowires or Ag foil as Ag precursor. The thickness of AgX shells can be adjusted by changing the molar ratio of $FeCl_3$ to Ag. By selecting polyvinyl pyrrolidone (PVP) as capping agent, cubic/cubic-like AgX ($X = Cl$, Br) nano- or microcrystals can be synthesized by hydrothemal, microemulsion, and sonochemical methods. AgX crystals with highly active facets can be tailored by selecting suitable capping agent (ionic liquids (ILs), PVP), together with controlling the concentrations of Ag^+ and X^- ions. Moreover, this review briefly reviewed the photocatalytic mechanism and applications of AgX (Ag/AgX) and supported AgX materials. For Ag/AgCl photocatalyst, the visible light phocatalytic activity is mainly relative to the plasmonic absorption of Ag narnoparticles. In the case of Ag/AgBr and Ag/AgI, both Ag nanoparticles and AgX can response to visible light irradiation. Photogenerated holes (h^+) and electrons (e^-) can further react with H_2O, OH^-, X^-, and O_2 to produce reactive active species such as X^0, $OH^\bullet$, H_2O_2, and ${}^\bullet O_2{}^-$, which take part in the photocatalytic reactions.

Acknowledgments This work has been supported by the National Natural Science Foundation of China (21277046, 21047002, 20977030, 21173077), National Basic Research Program of China (973 Program, 2010CB732306), the Shanghai Natural Science Foundation (10ZR1407400), the Project of International Cooperation of the Ministry of Science and Technology of China (2011DFA50530), and the Science and Technology Commission of Shanghai Municipality (12XD1402200 and 10JC1403900) and the Fundamental Research Funds for the Central Universities.

References

1. Fujishima A, Honda KK (1972) Nature 238:237
2. Tsuji I, Kato H, Kudo A (2005) Angew Chem Int Ed 44:3565
3. Akihiko K, Yugo M (2009) Chem Soc Rev 38:253
4. Tong H, Ouyang SX, Bi YP, Umezawa N, Oshikiri M, Ye JH (2012) Adv Mater 24:229
5. Zhang Q, Lima DQ, Lee I, Zaera F, Chi MF, Yin YD (2011) Angew Chem Int Ed 50:7088
6. Bavykin DV, Friedrich JM, Walsh FC (2006) Adv Mater 18:2807
7. Mo JH, Zhang YP, Xu QJ, Lamson JJ, Zhao RY (2009) Atmo Environ 43:2229
8. Hwang J-S, Chang J-S, Park S-E, Ikeue K, Anpo M (2005) Top Catal 35:311
9. Sato S, Morikawa T, Saeki S, Kajino T, Motohiro T (2010) Angew Chem Int Ed 49:5101
10. Kakuta N, Goto N, Ohwaki H, Mizushima T (1999) J Phys Chem B 103:5917
11. Schürch D, Currao A, Sarkar S, Hodes G, Calzaferri G (2002) J Phys Chem B 106:12764
12. Pfanner K, Gfeller N, Calzaferri G (1996) J Photochem Photobio A 95:175
13. Yamashita Y, Aoyama N, Takezawa N, Yoshida K (1999) J Mol Catal A-Chem 150:233
14. Andersson M, Birkedal H, Franklin NR, Ostomel T, Boettcher S, Palmqvist AEC, Stucky GD (2005) Chem Mater 17:1409
15. Hu C, Lan Y, Qu J, Hu X, Wang A (2006) J Phys Chem B 110:4066
16. Klabunde KJ, Rodrigues S, Uma S, Martyanov IN (2005) J Catal 233:405
17. Hu C, Hu X, Wang X, Qu LS, Wang JH (2006) Environ Sci Technol 40:7903
18. Elahifard MR, Rahimnejad S, Haghighi S, Gholami MR (2007) J Am Chem Soc 129:9552
19. Hu C, Peng T, Hu X, Nie Y, Zhou X, Qu J, He H (2010) J Am Chem Soc 132:857
20. Wang P, Huang BB, Qin XY, Zhang XY, Dai Y, Whangbo MH (2009) Inorg Chem 48:10697
21. An CH, Wang RP, Wang ST, Zhang XY (2011) J Mater Chem 21:11532
22. Liang H, Yang H, Wang W, Li J, Xu H (2009) J Am Chem Soc 131:6068
23. Awazu K, Fujimaki M, Rockstuhl C, Tominaga J, Murakami H, Ohki Y, Yoshida N, Watanabe T (2008) J Am Chem Soc 130:1676
24. Wang P, Huang BB, Qin XY, Zhang XY, Dai Y, Wei JY, Whangbo M (2008) Angew Chem Int Ed 47:7931
25. Wang P, Huang BB, Zhang XY, Qin XY, Jin H, Dai Y, Wang ZY, Wei JY, Zhan J, Wang SY, Wang JP, Whangbo M-H (2009) Chem Eur J 15:1821
26. Bi YP, Ye JH (2009) Chem Commun 43:6551
27. Bi YP, Ye JH (2010) Chem Eur J 16:10327
28. Bai J, Li YX, Zhang CQ, Liang XF, Yang QB (2008) Colloid Surf A 329:165
29. Wang DS, Duan YD, Luo QZ, Li XY, Bao LL (2011) Desalination 270:174
30. Zhu MS, Chen PL, Liu MH (2011) J Mater Chem 21:16413
31. Chen DL, Yoo SH, Huang QS, Ali G, Cho SO (2012) Chem Eur J 18:5192
32. Kuai L, Geng BY, Chen XT, Zhao YY, Luo YC (2010) Langmuir 26:18723
33. Li YY, Ding Y (2010) J Phys Chem C 114:3175
34. Wang H, Gao J, Guo TQ, Wang RM, Guo L, Liu Y, Li JH (2012) Chem Commun 48:275
35. Lou ZZ, Huang BB, Qin XY, Zhang XY, Cheng HF, Liu YY, Wang SY, Wang JP, Dai Y (2012) Chem Commun 48:3488
36. Ye JF, Qi LM (2008) J Mater Sci Technol 24:529
37. Barth JV, Costantini G, Kern K (2005) Nature 437:671
38. Fan HJ, Werner P, Zacharias M (2006) Small 2:700
39. Lu W, Lieber CM (2007) Nat Mater 6:841
40. Cozzoli PD, Kornowski A, Weller H (2003) J Am Chem Soc 125(47):14539
41. Wu HB, Hng HH, Lou XW (2012) Advan Mater 24:2567
42. Tong H, Zhu YJ, Yang LX, Li L, Zhang L (2006) Angew Chem Int Edit 45:7739
43. Cao BL, Jiang Y, Wang C, Wang WH, Wang LZ, Niu M, Zhang WJ, Li YQ, Lee ST (2007) Adv Func Mater 17:1501
44. Zhan J, Yang X, Wang D, Li S, Xie Y, Xia Y, Qian Y (2000) Adv Mater 12:1348
45. Xu D, Liu Z, Liang J, Qian Y (2005) J Phys Chem B 109:14344
46. Ouyang L, Maher KN, Yu CL, McCarty J, Park HK (2007) J Am Chem Soc 129:133
47. Saliby EI, Okour Y, Shon HK, Kandasamy J, Lee WE, Kim J-H (2012) J Ind Eng Chem 18(3):1033
48. Pyne S, Sahoo GP, Bhui DK, Bar H, Sarkar P, Samanta S, Maity A, Misra A (2012) Spectrochim Acta A 93:100
49. Liu ZF, Zhang QH, Li YG, Wang HZ (2012) J Phys Chem Solids 73:651
50. Liu XQ, Li Z, Zhang Q, Li F, Kong T (2012) Mater Lett 72:49
51. Lu XH, Zhai T, Cui HN, Shi JY, Xie SL, Huang YY, Liang CL, Tong YX (2011) J Mater Chem 21(15):5569
52. Lü XJ, Ding SJ, Lin TQ, Mou XL (2012) Dalton Trans 41:622
53. Li YX, Hu YF, Peng SQ, Lu GX, Li SB (2009) J Phys Chem C 113:9352
54. Wu T, Zhou XG, Zhang H, Zhong XH (2010) Nano Res 3:379
55. Han QF, Chen L, Wang MJ, Yang XJ, Lu LD, Wang X (2010) Mater Sci Eng, B 166:118

56. Chen LL, Zhang WX, Feng C, Yang ZH, Yang YM (2012) Ind Eng Chem Res 51:4208
57. Chen Y, Liu GC, Yang J-T, Wei Q-M (2011) Chin J Inorg Chem 27:1059
58. Bi YP, Lu GX (2008) Chem Commun 47:6402
59. Bi YP, Lu GX (2008) Nanotechnol 19:275306
60. Bi YP, Lu GX (2008) Chem Mater 20:1224
61. Zhao D, Yan B, Xu B (2008) Electrochem Commun 10:884
62. Sun YG (2010) J Phys Chem C 114:2127
63. Li F, Liu XQ, Yuan YL, Wu JF, Li Z (2010) Cryst Res Tech 45(11):1189
64. Liu XQ, Li Z, Li F, Qin QH (2012) Mater Res Bull 47:1285
65. Xia Y, Xiong Y, Lim B, Skrabalak SE (2009) Angew Chem Int Ed 48:60
66. Chen J, Lim B, Lee EP, Xia Y (2009) Nano Today 4:81
67. An CH, Peng S, Sun YG (2010) Adv Mater 22:2570
68. Han L, Wang P, Zhu CZ, Zhai YM, Dong SJ (2011) Nanoscale 3:2931
69. Yan ZJ, Compagnini G, Chrisey DB (2011) J Phys Chem C 115:5058
70. Ganguli AK, Ganguly A, Vaidya S (2010) Chem Soc Rev 39:474
71. Liu G, Yu JC, Lu GQ, Cheng HM (2011) Chem Commun 47:6763
72. Gong XQ, Selloni A (2005) J Phys Chem B 109:19560
73. Selloni A (2008) Nat Mater 7:613
74. Vittadini A, Casarin M, Selloni A (2006) Theor Chem Acc 117:663
75. Pan J, Liu G, Lu GQ, Cheng HM (2011) Angew Chem Int Ed 50:2133
76. Yu H, Tian BZ, Zhang JL (2011) Chem Eur J 17:5499
77. Yang HG, Sun CH, Qiao SZ, Zou J, Liu G, Smith SC, Cheng HM, Lu GQ (2008) Nature 453:638
78. Liu G, Yang HG, Wang XW, Cheng LN, Pan J, Lu GQ, Cheng HM (2009) J Am Chem Soc 131:12868
79. Zhang DQ, Li GS, Yu JC (2009) Chem Commun 45:4381
80. Wang XN, Huang BB, Wang ZY, Qin XY, Zhang XY, Dai Y, Whangbo MH (2010) Chem Eur J 16:7106
81. Liu SW, Yu JG, Jaroniec M (2010) J Am Chem Soc 132:11914
82. Liu SW, Yu JG, Jaroniec M (2011) Chem Mater 23:4085
83. Zeng JH, Jin BB, Wang YF (2009) Chem Phys Lett 472:90
84. Mclaren A, Valdes-Solis T, Li GQ, Tsang SC (2009) J Am Chem Soc 131:12540
85. Zhou WW, Yan B, Cheng CW, Cong CX, Hu HL, Fan HJ, Yu T (2009) Cryst Eng Comm 11:2291
86. Zhang Y, Deng B, Zhang TR, Gao DM, Xu AW (2010) J Phys Chem C 114:5073
87. Zhao ZG, Liu ZF, Miyauchi M (2010) Chem Commun 46:3321
88. Bi YP, Quyang SX, Umezawa N, Cao JY, Ye JH (2011) J Am Chem Soc 133:6490
89. Wang H, Lang XF, Gao J, Liu W, Wu D, Wu YM, Guo L, Li JL (2012) Chem Eur J 18:4620
90. Lou ZZ, Huang BB, Wang P, Wang ZY, Qin XY, Zhang XY, Cheng HF, Zheng ZK, Dai Y (2011) Dalton Trans 40:4104
91. Lou ZZ, Huang BB, Qin XY, Zhang XY, Wang ZY, Zheng ZK, Cheng HF, Wang P, Dai Y (2011) CrystEngComm 13:1789
92. Wang W, Lu WS, Jiang L (2009) J Colloid Interface Sci 338:270
93. Yang M, Zhou K (2011) Appl Surf Sci 257:2503
94. He CX, Tian BZ, Zhang JL (2010) J Colloid Interf Sci 344:382
95. Yang M, Zhao J-G, Li J-J (2007) Colloid Surf A 295:81
96. Wang P, Huang BB, Lou ZZ, Zhang XY, Qin XY, Dai Y, Zheng ZK, Wang XN (2010) Chem Eur J 16:538
97. An CH, Wang JZ, Qin C, Jiang W, Wang ST, Li Y, Zhang QH (2012) J Mater Chem 22:13153
98. Peng S, Sun YG (2011) J Mater Chem 21:11644
99. Liu L, Xu H, Li HM, Xu YG, Xia JX, Yin S (2012) J Physics Chem Solids 73:523
100. Huang BB, Wang P, Zhang XY, Qin XY, Dai Y, Wang ZY, Lou ZZ (2011) ChemCatChem 3:360
101. Jiang J, Zhang LZ (2011) Chem Eur J 17:3710
102. Xu H, Li HM, Xia JX, Yin S, Luo ZJ, Liu L, Xu L (2011) ACS Appl Mater Interface 3:22
103. Lei JY, Wang W, Song MX, Dong B, Li ZY, Wang C, Li LJ (2011) React Funct Polym 71:1071
104. Farnood R, Zang YJ, Currie J (2009) Chem Eng Sci 64:2881
105. Li GT, Wong KH, Zhang XW, Hu C, Yu JC, Chan RCY, Wong PK (2009) Chemosphere 76:1185
106. Zhang XJ, Li JL, Lu X, CQ T, Lu GX (2012) J Colloid Interf Sci 377:277
107. An CH, Ming XJ, Wang JZ, Wang ST (2012) J Mater Chem 22:5171
108. Guo JF, Ma BW, Yin AY, Fan KN, Dai WL (2011) Appl Catal B-Environ 101:580
109. Sohrabnezhad S, Pourahmad A (2012) Spectrochim Acta Pt A 86:271
110. Pourahmad A, Sohrabnezhad Sh, Kashefian E (2010) Spectrochimica Acta Part A 77:1108
111. Ma BW, Guo JF, Zou LY, Dai WL, Fan KN (2011) Chin J Chem 29:857
112. Hu C, Zhou XF, Hu XX, Peng TW, Qu JH (2010) J Phys Chem C 114:2746
113. Zhao YY, Kuai L, Geng BY (2012) Catal Sci Technol 2:1269
114. Ashokkumar M, Marignier JL (1999) Int J Hydrogen Energ 24:17
115. Calzaferri G, Lanz M, Schurch D (1999) J Photochem Photobiol A: Chem 120:105
116. Reddy VR, Currao A, Calzaferri G (2007) J Mater Chem 17:3603
117. Lanz M, Calzaferri G (1997) J Photochem Photobiol A-Chem 109:87
118. Hu C, Hu XX, Peng TW, Zhou XF, Qu JH (2010) Environ Sci Technol 44:7058
119. Lan YQ, Hu C, Hu XX, Qu JH (2007) Appl Catal B 73:354
120. Carp O, Huisman CL, Reller A (2004) Prog Solid State Chem 32:33
121. Fujishima A, Zhang XT, Tryk DA (2008) Surf Sci Rep 63:515
122. Huang XH, El-Sayed MA (2010) J Adv Res 1:13
123. Papavassiliou GC (1979) Prog Solid State Chem 12:185
124. Linic S, Christopher P, Ingram DB (2011) Nat Mater 10:911
125. Kowalska E, Abe R, Ohtani B (2009) Chem Comm 2:241
126. Tian Y, Tatsuma T (2004) Chem Comm 16:1810
127. Ingram DB, Linic S (2011) J Am Chem Soc 133:5202
128. Liu Z, Hou W, Pavaskar P, Aykol M, Cronin SB (2011) Nano Lett 11:1111
129. Primo A, Marino T, Corma A, Molinari R, García H (2011) J Am Chem Soc 133:6930
130. Victora RH (1997) Phys. Rev. B 56:4417
131. Atkins PW (1990) Physical Chemistry, 4th edn. Oxford University Press, Oxford
132. Baur E, Rebmann A (1921) Helv Chim Acta 4:256
133. Metzner H (1968) Hoppe-Seyler's. Z Physiol Chem 349:1586
134. Metzner H, Fischer K (1974) Photosynthetica 8:257
135. Metzner H, Fischer K, Lupp G (1975) Photosynthetica 9:327
136. Chandrasekaran K, Thomas JK (1983) Chem Phys Lett 97:357
137. Calzaferri G, Spahni W (1986) J Photochem 32:151
138. Calzaferri G, Spahni W (1986) Chimia 40:435
139. Beer R, Calzaferri G, Spahni W (1988) Chimia 42:134
140. Calzaferri G, Spahni W (1987) Chimia 41:200
141. Beer R, Binder F, Calzaferri G (1992) J Photochem Photobiol A 69:67

142. Calzaferri G, Gfeller N, Pfanner K (1995) J Photochem Photobiol A 87:81
143. Saladin F, Kamber I, Pfanner K, Calzaferri G (1997) J Photochem Photobiol A 109:47
144. Slamet Nasution HW, Nasution Purnama E, Kosela S, Gunlazuardi J (2005) Catal Commun 6:313
145. Pan PW, Chen YW (200) Catal Commun 8:1546
146. Zhang QH, Han WD, Hong YJ, Yu JG (2009) Catal Today 148:335
147. Asi MA, He C, Su MH, Xia DH, Lin L, Deng HQ, Xiong Y, Qiu RL, Li XZ (2011) Catal Today 175:256
148. Hu C, Guo J, Qu JH, Hu XX (2007) Langmuir 23:4982
149. Zhang LS, Wong KH, Yip HY, Hu C, Yu JC, Chan CY, Wong PK (2010) Environ Sci Technol 44:1392
150. Hou Y, Li XY, Zhao QD, Chen GH, Raston CL (2012) Environ Sci Technol 46:4042